



**HAL**  
open science

# A hyperbolic phase-transition model coupled to tabulated EoS for two-phase flows in fast depressurizations

M. de Lorenzo, Ph. Lafon, M. Pelanti, A. Pantano, M. Di Matteo, Y. Bartosiewicz, J.-M. Seynhaeve

## ► To cite this version:

M. de Lorenzo, Ph. Lafon, M. Pelanti, A. Pantano, M. Di Matteo, et al.. A hyperbolic phase-transition model coupled to tabulated EoS for two-phase flows in fast depressurizations. Nuclear Engineering and Design, 2021, 371, pp.110954 -. 10.1016/j.nucengdes.2020.110954 . hal-03492966

**HAL Id: hal-03492966**

**<https://hal.science/hal-03492966>**

Submitted on 15 Dec 2022

**HAL** is a multi-disciplinary open access archive for the deposit and dissemination of scientific research documents, whether they are published or not. The documents may come from teaching and research institutions in France or abroad, or from public or private research centers.

L'archive ouverte pluridisciplinaire **HAL**, est destinée au dépôt et à la diffusion de documents scientifiques de niveau recherche, publiés ou non, émanant des établissements d'enseignement et de recherche français ou étrangers, des laboratoires publics ou privés.



Distributed under a Creative Commons Attribution - NonCommercial 4.0 International License

## A hyperbolic phase-transition model coupled to tabulated EoS for two-phase flows in fast depressurizations

M. De Lorenzo<sup>a,\*</sup>, Ph. Lafon<sup>a</sup>, M. Pelanti<sup>a</sup>, A. Pantano<sup>a,b,c</sup>, M. Di Matteo<sup>d</sup>, Y. Bartosiewicz<sup>d</sup>, J.-M. Seynhaeve<sup>d</sup>

<sup>a</sup>IMSIA UMR EDF-CNRS-CEA-ENSTA, Palaiseau, France 91120

<sup>b</sup>Politecnico di Torino, Torino, Italy 10129

<sup>c</sup>INP Phelma, Grenoble, France 38000

<sup>d</sup>Université catholique de Louvain (UCL), Institute of Mechanics, Materials, and Civil Engineering (iMMC), Louvain la Neuve, Belgium 1348

---

### Abstract

This article deals with a single-velocity six-equation two-phase flow model and its use for the simulation of metastable liquid-vapor flows of industrial interest like fast depressurizations in which phases are in thermo-chemical disequilibrium.

The purpose of this work is to develop a numerical method of industrial grade with enhanced adherence to physics by employing advanced modeling techniques based on hyperbolic multiphase flow models proposed in the last two decades. The model here developed is able to accurately take into account disequilibrium between phases thanks to splitted relaxation processes for pressure, temperature and Gibbs free enthalpy disequilibria. At the same time, numerical calculations rely on fast and accurate Equations of State (EoS).

To obtain such a tool, in this paper, we merge the single-velocity six-equation two-phase flow model with novel relaxation procedures and steam-water tables calculation methods. The outcome is an accurate and time-efficient hyperbolic model for simulating metastable two-phase flows. The merging builds up on previous work of the authors that was dedicated on the one hand to EoS-independent relaxation procedures for the six-equation model, and on the other hand on steam-water look-up table techniques coupled to simpler two-phase flow models.

Since the single-velocity six-equation model is capable of accounting for vapor metastable states, the steam-water tables and the look-up table technique that we developed in previous work are extended here to the vapor metastable domain up to the vapor spinodal line. Then, the complete six-equation model is coupled to the new steam-water tables for the simulation of metastable two-phase flows occurring in the event of a fast depressurization. These simulations are validated against experimental data available in the literature.

The final model is implemented in the EUROPLEXUS code for its use in nuclear reactor safety.

*Keywords:* two-phase flow; relaxation procedures; tabulated equations of state; metastable states; fast transients; depressurizations.

## Nomenclature

### Latin Letters

$A$	Area
$\mathbf{B}$	Non-conservative product vector
$C$	Specific heat
$c$	Speed sound
$E$	Specific total energy
$e$	Specific internal energy
$f$	Specific Helmholtz free energy
$g$	Specific Gibbs free enthalpy
$G_{1\rightarrow 2}$	Phase transition mass flow rate
$H$	Non-conservative product discrete terms
$h$	Heat transfer coefficient
$a, b, i, j, k$	Relaxation coefficients
$K$	Mass fraction parameter
$L$	Operator
$m$	Partial density
$p$	Pressure
$S$	Entropy
$S$	Wave speed
$s$	Specific Entropy
$T$	Temperature
$t$	Time
$\mathbf{U}$	Calculation variable vector
$u$	Mixture velocity
$V$	Volume
$v$	Specific volume
$X, Y$	Cartesian coordinates
$Y$	Mass fraction
$z$	Spatial coordinate

---

\*Corresponding author  
Email address: marco.vibo@icloud.com (M. De Lorenzo)

## Greek Letters

$\alpha$	Volume fraction
$\alpha, \beta$	Bilinear mapping coefficients
$\Delta$	Interval
$\Gamma$	Grüneisen coefficient
$\lambda$	Eigenvalue
$\rho$	Density
$\Sigma$	Non-conservative products
$\Theta$	Characteristic time

## Subscripts

<i>conv</i>	Convection
<i>l</i>	Left
<i>hom</i>	Homogeneous
<i>hyp</i>	Hyperbolic
<i>int</i>	Interfacial
<i>l</i>	Liquid phase
<i>r</i>	Right
<i>sat</i>	At saturation conditions
<i>v</i>	Vapor phase

## 1. Introduction

The last two decades have seen a great improvement in the mathematical and numerical modeling of two-phase flows. Hyperbolic models have become more popular and their application domains are various. These advancements led to a better description of the disequilibria phenomena existing between phases. In this context an effective modeling approach consists in decomposing thermodynamic disequilibrium in mechanical, thermal and chemical disequilibrium processes.

In case of phase transition simulations of a single-component mixture, the occurrence of thermodynamic disequilibrium may lead to the presence of metastable states, that is, the persistence of a phase into the stability domain of another phase. Thanks to the contribution of new techniques based on hyperbolic flow models, the analysis of metastable two-phase flows has greatly improved. Nonetheless, these improvements

have not changed the numerical methodologies of common use in industry.

One of the reasons stems from the difficulty of using real equations of state in some of the recent and more advanced approaches. The numerical techniques recently proposed in the literature [11, 38, 49, 50, 64] are often designed only for very simple Equations of State (EoS) as the stiffened gas one. However, this is not adequate for some industrial applications.

Our research is fully devoted to the nuclear reactor safety in Pressurized Water Reactors (PWRs), where the coolant is the water. Due to highly non-linear behaviors of water, engineers and the nuclear regulator are often skeptical about the use of simplistic EoS. For this reason, we paid a tremendous attention to the capability to use accurate EoS. Our approach is different because, conversely to many other research works in the hyperbolic domain, we built the whole numerical model around a tabulated EoS. This is dictated by our industrial needs. As a result, some of our modeling choices are constrained.

One of the main reasons that led us to develop the single-velocity six-equation two-phase flow model stems from this constraint. In fact, aside from the seven-equation model, this is the only model with a full thermodynamic separation between the two phases. As we will see in the next section, this model requires two phasic EoS totally independent from each other.

In all other models, thermodynamic closure laws are somehow dependent from each other. When using a simple EoS as the stiffened gas one, this is not an issue because closure laws are so simple that can be analytically manipulated to end up in a simple analytic law, e.g. [8, 12, 29, 49]. By contrast, when using real EoS or tabulated ones, this is not possible and a non-linear algebraic equation must be iteratively solved to guarantee the equality of phasic pressures and/or temperatures. Solving this non-linear equation per each cell at every time step is extremely time-consuming and can also lead to low robustness of the whole numerical model. We experienced this problem in the HRM in [17], other authors experienced it using the single-pressure six-equation model in conservative variables [55], and the same problem would be encountered if the Kapila model [31] was coupled to a real EoS.

Therefore, the choice of the single-velocity six-equation two-phase flow model allows us to use tabulated EoS avoiding any iterative method. In this way, we have both an accurate thermodynamic modeling and a greater robustness, both features are fundamental for our industrial scope.

Our previous works separately dealt with the fluid properties calculation and the single-velocity six-equation two-phase flow model. In [17], we developed a fast and accurate technique for the calculation of steam-water properties. Then, in [18], we verified the hyperbolic solver and analyzed the integration of non-conservative terms. Later, in [19], we proposed a novel method for the relaxation of thermodynamic disequilibrium for phases described by arbitrary EoS.

The purpose of the current work is to couple the three aforementioned techniques to simulate metastable two-phase flows of industrial concern as fast depressurizations in which phases are in thermo-chemical disequilibrium. The outcome of this work is a hyperbolic model for metastable two-phase flows that uses

the proposed techniques for the calculation of interfacial transfers and steam-water properties. Moreover, it is computationally affordable for its use in industrial configurations.

In our previous works, the single-velocity six-equation model was numerically integrated using the basic Fortran libraries of the CLAWPACK software [35]. [Due to its industrial interest, we have now implemented it in EUROPLEXUS code \[25\] for the simulation of metastable steam-water flows for nuclear reactor safety analyses. In this paper, we use our methodology for simulating fast depressurizations, validating it against experimental data available in the literature.](#)

The outline of the article is the following. In Section 2 we briefly describe the single-velocity six-equation two-phase flow model together with its physical and mathematical properties. Here we discuss both the homogeneous hyperbolic portion of the model and the source terms necessary for the thermodynamic equilibrium recovery. Section 3 explains our strategy for the calculation of steam-water properties and the developments of the work done in [17] to extend it to metastable vapor states. In Section 4 we show the numerical methods developed to integrate the complete model, focusing on Riemann and Runge–Kutta solvers.

These methods are used in Section 5 in tests of industrial grade in which we compare the computational results of the complete model to several fast depressurizations experiments realized in steam-water systems. Finally, in Section 6, we give some conclusions and perspectives.

## 2. Single-velocity six-equation two-phase flow model

For the metastable two-phase flows simulation, we chose the single-velocity six-equation model [31, 50] in the form proposed in [38] to ensure *mixture-energy-consistency* at discrete level. The six-equation model is a two-phase two-pressure system modeling the dynamics of mixture of fluids that can also deal with phase transitions when phases are the liquid and its vapor.

[It is a reduced model of the seven-equation model \[2\] in which phases are constrained to move at the same velocity. This is a strong assumption in two-phase flow because very often phases move at a significantly different speed. However, this assumption is here justified by the fact that our research purpose is the description of the very first milliseconds of rapid depressurizations, the so-called acoustic phase, where thermodynamic disequilibria play the most important role as we can see in Bartak’s experimental campaign \[3, 54\].](#)

[Our research is only devoted to the acoustic phase of fast depressurizations because our main industrial interest is the analysis of the fluid-structure interaction in reactor cores caused by the rarefaction wave originated at the breach at the very beginning of a Loss-of-Coolant Accident \(LOCA\). By contrast, to analyze the subsequent evolution of a LOCA, it is necessary to use a two-fluid model to allow phases to move at different velocity.](#)

In the following, first we introduce the homogeneous hyperbolic portion of the model, then we describe the complete model proposed by the authors in [19].

### 2.1. Homogeneous hyperbolic portion of the model

The governing equations consist of mass and energy balance laws for each phase, a momentum balance for the mixture, plus an advection equation for one of the two phases. In 1D, the hyperbolic homogeneous portion of this model reads

$$\begin{cases} \partial_t \alpha_1 + u \partial_z \alpha_1 = 0, \\ \partial_t(\alpha_1 \rho_1) + \partial_z(\alpha_1 \rho_1 u) = 0, \\ \partial_t(\alpha_2 \rho_2) + \partial_z(\alpha_2 \rho_2 u) = 0, \\ \partial_t(\rho u) + \partial_z(\rho u^2 + \alpha_1 p_1 + \alpha_2 p_2) = 0, \\ \partial_t(\alpha_1 \rho_1 E_1) + \partial_z[\alpha_1(\rho_1 E_1 + p_1)u] + \Sigma = 0, \\ \partial_t(\alpha_2 \rho_2 E_2) + \partial_z[\alpha_2(\rho_2 E_2 + p_2)u] - \Sigma = 0. \end{cases} \quad (1)$$

At each phase is assigned a density  $\rho_k$ , a pressure  $p_k$ , a specific internal energy  $e_k$  and a volume fraction  $\alpha_k$ , where  $k = 1, 2$ .  $E_k = e_k + \frac{1}{2}u^2$  are the specific total energies and  $\rho = \alpha_1 \rho_1 + \alpha_2 \rho_2$  is the mixture density. Both phases move at velocity  $u$ . Two other useful quantities are: phasic mass fractions  $Y_k = \alpha_k \rho_k / \rho$  and phasic partial densities  $m_k = \alpha_k \rho_k$ . The volume saturation condition  $\alpha_1 + \alpha_2 = 1$  is obviously assumed.

The non-conservative terms appearing in phasic total energy equations are

$$\Sigma = -u \cdot [Y_2 \partial_z(\alpha_1 p_1) - Y_1 \partial_z(\alpha_2 p_2)]. \quad (2)$$

These terms are non-zero if  $u \neq 0$  and if  $Y_1 Y_2 \neq 0$ , that is, if the fluid is a mixture containing both species moving at non-zero velocity.

The above system of partial differential equations is hyperbolic and its eigenvalues are

$$\lambda_1 = u - c_{hom}, \quad \lambda_{2,\dots,5} = u, \quad \lambda_6 = u + c_{hom}, \quad (3)$$

where the speed of sound of the associated homogeneous model is

$$c_{hom} = \sqrt{Y_1 c_1^2 + Y_2 c_2^2}, \quad (4)$$

and  $c_k$  are the phasic isentropic speeds of sound. In order to close the system, two equations of state (EoS) are needed, one per each phase. They are of the form of *incomplete EoS* [10]:

$$p_k = p_k(\rho_k, e_k). \quad (5)$$

In this work, we do not use an analytic relation for (5), rather a look-up table algorithm for a fast and accurate evaluation of steam-water properties [17]. This procedure provides bicubic spline functions globally continuous on the entire  $e$ - $v$  domain. This technique is explained in Section 3.

## 2.2. The complete model for phase transition

The complete single-velocity six-equation two-phase flow model proposed in [19] allows us to simulate phase transition phenomena of metastable phases. Relaxation processes are non-instantaneous and phases can be described by arbitrary EoS. As shown by the authors in [19] and previously discussed in [56] for another flow model, when equilibrium recovery mechanisms are assumed to be quasi-instantaneous, the six-equation model tends to the Homogeneous Equilibrium Model (HEM), that is, infinitely fast relaxation mechanisms can not simulate metastable flows.

The model and the numerical procedures we proposed in [19] have the capability to describe an arbitrarily fast equilibrium recovery. This enables to correctly simulate metastable two-phase flows. The numerical procedures proposed in [19] enable to separately account for the three main physical processes that drive a metastable mixture towards equilibrium. These processes are: (i) compression-expansion energy transfer leading to phasic pressures equilibrium, also called *pressure relaxation process*, (ii) sensible heat transfer, also called *temperature relaxation process*, and (iii) mass transfer process occurring during a phase transition.

Considering the contribution of the relaxation sources, the six-equation model reported in Eq. (1) becomes:

$$\left\{ \begin{array}{l} \partial_t \alpha_1 + u \partial_z \alpha_1 = \frac{\alpha_1}{a \rho_1 \Theta^p} (p_1 - p_2) + \frac{\alpha_1}{a \rho_1} \frac{h A_{int}}{V} (T_1 - T_2) - \frac{1}{\rho_1} \left( 1 - \alpha_1 \frac{i_p k_T - k_p i_T}{k_p j_T - j_p k_T} \right) G_{1 \rightarrow 2} \frac{A_{int}}{V}, \\ \partial_t (\alpha_1 \rho_1) + \partial_z (\alpha_1 \rho_1 u) = -G_{1 \rightarrow 2} \frac{A_{int}}{V}, \\ \partial_t (\alpha_2 \rho_2) + \partial_z (\alpha_2 \rho_2 u) = +G_{1 \rightarrow 2} \frac{A_{int}}{V}, \\ \partial_t (\rho u) + \partial_z (\rho u^2 + \alpha_1 p_1 + \alpha_2 p_2) = 0, \\ \partial_t (\alpha_1 \rho_1 E_1) + \partial_z [\alpha_1 (\rho_1 E_1 + p_1) u] + \Sigma = -\frac{\alpha_1 p_{int}}{a \rho_1 \Theta^p} (p_1 - p_2) + b_T \frac{h A_{int}}{V} (T_1 - T_2) - b_g G_{1 \rightarrow 2} \frac{A_{int}}{V}, \\ \partial_t (\alpha_2 \rho_2 E_2) + \partial_z [\alpha_2 (\rho_2 E_2 + p_2) u] - \Sigma = +\frac{\alpha_1 p_{int}}{a \rho_1 \Theta^p} (p_1 - p_2) - b_T \frac{h A_{int}}{V} (T_1 - T_2) + b_g G_{1 \rightarrow 2} \frac{A_{int}}{V}, \end{array} \right. \quad (6)$$

where  $p_{int}$  denotes an averaged interface pressure that here we define as in [46],

$$p_{int} = \alpha_1 p_1 + \alpha_2 p_2 \quad (7)$$

and does not account for curvature and surface tension effects, which are considered negligible. Other definitions are possible, e.g. [9, 47]. The other terms introduced in [19] are:

$$b_T = \alpha_1 \rho_1 \left[ \frac{p_{int}}{a \rho_1^2} \left( \frac{\Gamma_1}{\alpha_1} + \frac{\Gamma_2}{\alpha_2} \right) - \frac{1}{\alpha_1 \rho_1} \right], \quad b_g = \alpha_1 \rho_1 \frac{j_p i_T - i_p j_T}{k_p j_T - j_p k_T} \quad (8)$$

The form of the thermal relaxation terms appearing in the energy equations and in the volume fraction equation allows us to maintain constant the phasic pressure difference during the temperature relaxation process. Analogously, the form of the mass transfer terms in those three equations keeps constant the pressure and temperature difference during a phase transition process [19]. These enable to strictly separate the



three relaxation mechanisms and to prevent non-physical behaviors. The definitions of  $i_p, j_p, k_p, i_T, j_T$  and  $k_T$  can be found in Appendix A.

$A_{int}/V$  is the interfacial area density per unit volume. It is a very important quantity because interphasic transfers occur at the interface and are proportional to interfacial area. At the current state of our research we have set it to unity, but we expect to improve our modeling using a separate flow-pattern model to better estimate this quantity.

$h$  is the convection heat transfer coefficient,  $\Gamma_k$  are the phasic Grüneisen coefficients, and  $\Theta^p$  is the characteristic time for pressure equilibrium recovery.

From (6) we can see that pressure disequilibrium ( $p_1 - p_2$ ) drives the compression-expansion energy transfer in pressure relaxation process. The term  $(T_1 - T_2)$  drives the sensible heat transfer. This is a simplification of the real phenomenon because the sensible heat transfer in each phase is not driven by phasic temperature difference but by their differences with respect to interfacial temperature.  $G_{1 \rightarrow 2}$  stands for the net mass flow rate per unit interfacial area due to phase transition phenomena.

Source terms standing on the right-hand-side of Eq. (6) represent the mathematical modeling of physical phenomena occurring during a phase transition. These phenomena are irreversible, then they lead to an increase of the mixture entropy. The irreversibility of such phenomena is discussed in Appendix B.

### 3. Look-up table algorithm for liquid and vapor EoS

To correctly simulate phase transition phenomena, accurate equations of state should be used. For the steam-water properties, nowadays, the most reliable EoS for water is the IAPWS-95 [60]. This is an analytical equation based on experimental data and is used for general and scientific purposes. Given that the IAPWS-95 formulation is quite cumbersome and time consuming, IAPWS also provides a separate formulation recommended for industrial use, i.e. the IAPWS-IF97 [61]. The latter consists of a set of equations for five different regions, fitting the values resulting from the IAPWS-95. In this work we rely on the IAPWS-IF97 for the water properties calculation.

Generally, accurate EoS are expressed as:

$$f = f(\rho, T) \quad \text{or} \quad g = g(p, T), \quad (9)$$

where:  $f = e - Ts$  and  $g = h - Ts$  are, respectively, the Helmholtz free energy and the Gibbs free enthalpy. The IAPWS-IF97 is a combination of the these two forms because is composed of four EoS, each of which describes the water properties of a subdomain of the thermodynamic diagram. These subdomains are called

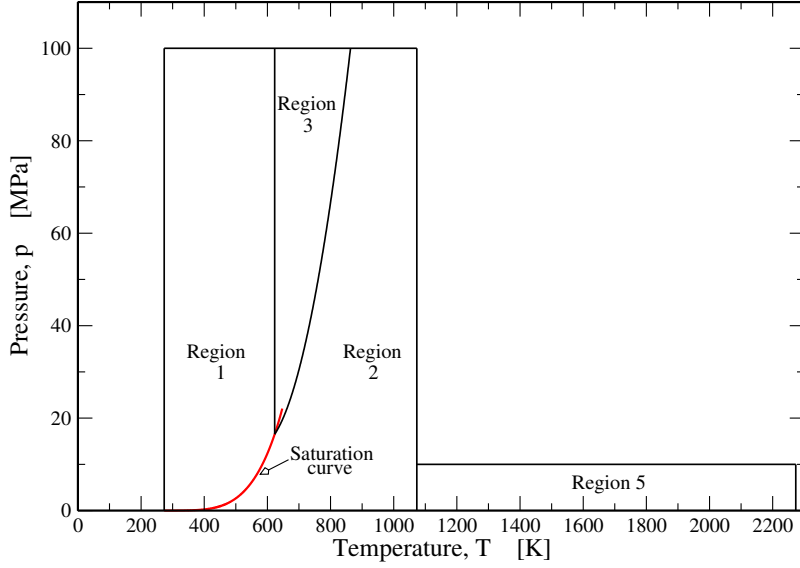


Figure 1: Region subdivision of the IAPWS-IF97 on the  $p$ - $T$  diagram. Region 4 represents the saturation curve.

regions and are depicted in Fig. 1. The IAPWS-IF97 EoS reads:

$$\text{for Region 1 : } g(p, T) = RT \left( \sum_{i=1}^{34} n_{1,i} (7.1 - \pi)^{I_{1,i}} (\tau - 1.222)^{J_{1,i}} \right), \quad (10a)$$

$$\text{for Region 2 : } g(p, T) = RT \left( \ln \pi + \sum_{i=1}^9 n_{2,i}^o \tau^{J_{2,i}^o} + \sum_{i=1}^{43} n_{2,i} \pi^{I_{2,i}} (\tau - 0.5)^{J_{2,i}} \right), \quad (10b)$$

$$\text{for Region 3 : } f(\rho, T) = RT \left( n_{3,1} \ln \delta + \sum_{i=2}^{40} n_{3,i} \delta^{I_{3,i}} \tau^{J_{1,i}} \right), \quad (10c)$$

$$\text{for Region 5 : } g(p, T) = RT \left( \ln \pi + \sum_{i=1}^6 n_{5,i}^o \tau^{J_{5,i}^o} + \sum_{i=1}^5 n_{5,i} \pi^{I_{5,i}} \tau^{J_{5,i}} \right). \quad (10d)$$

where  $R = 0.461526 \text{ kJ kg}^{-1} \text{ K}^{-1}$  is the specific gas constant of ordinary water,  $\pi$ ,  $\tau$  and  $\delta$  are the reduced pressure, temperature and density, that is, normalized values with respect to the critical point. The coefficients  $n_{k,i}$ ,  $I_{k,i}$  and  $J_{k,i}$  can be easily found in [61].

These EoS are very accurate for stable states because they are based on experimental data. However, they are not explicitly made to fit metastable condition data, therefore it is expected a lower accuracy in this domain.

Such EoS are very accurate but extremely costly from a computational point of view. Therefore, replacing the incomplete EoS in (5) by an iterative algorithm that implements a complete EoS as (9) is feasible but too expensive for industrial calculations. Further, the iterative algorithm may be an issue for the global robustness of the code since it may not converge.

Based on the works of Kunick et al. [33, 34], we proposed in [17] an alternative strategy to calculate steam-

water properties. In our previous work, it consisted in a look-up table method that calculates  $p = p(\rho, e)$  by a bicubic interpolation in the  $e$ - $v$  thermodynamic diagram. The choice of the  $e$ - $v$  diagram for the look-up table method comes from the fact that the specific volume  $v = 1/\rho$  and the specific internal energy  $e$  are immediately available from the vector of the conservative variables.

Since it was used for HEM and HRM calculations,  $\rho$  and  $e$  referred to single-phase states or to equilibrium mixture ones. For the current work, we developed a very similar technique but for the calculation of phasic EoS, i.e.  $p_k = p_k(\rho_k, e_k)$ , because those are required for the six-equation model (see Eq. (5)).

In the following we discuss the physical constraints for phasic EoS in order to identify the limits of the liquid and vapor domains. Then we present such domains on the  $e$ - $v$  diagram of water, showing the extension up to liquid and vapor spinodal curves. Finally, we recall the guidelines of our strategy for the bicubic interpolation of the thermodynamic properties.

### 3.1. Physical constraints of phasic EoS

For the current work, we have developed a bicubic spline method for the calculation of phasic EoS as:

$$p_k = p_k(\rho_k, e_k), \quad T_k = T_k(\rho_k, e_k), \quad g_k = g_k(\rho_k, e_k). \quad (11)$$

It means that the  $e$ - $v$  diagram has been divided into two domains: the *liquid domain* and the *vapor domain*. In the liquid domain, liquid EoS exist in the forms:

$$p_l = p_l(\rho_l, e_l), \quad T_l = T_l(\rho_l, e_l), \quad g_l = g_l(\rho_l, e_l), \quad (12)$$

and in the vapor domain, similarly, vapor EoS are:

$$p_v = p_v(\rho_v, e_v), \quad T_v = T_v(\rho_v, e_v), \quad g_v = g_v(\rho_v, e_v). \quad (13)$$

Since here we are dealing with phasic EoS, phasic domains are bounded by physical constraints of thermodynamic stability. For each phase, the criteria for equilibrium and stability [7] can be expressed, respectively, as:

$$\delta S_k = 0, \quad \delta^n S_k < 0 \quad \text{for the smallest } n \text{ at which } \delta^n S_k \neq 0, \quad (14)$$

where  $S_k$  are phasic entropies. Further developments of the last criterion provide two conditions which ensure thermodynamic stability of a system:

$$C_{v,k} > 0, \quad \left( \frac{\partial p_k}{\partial v_k} \right)_{T_k} < 0. \quad (15)$$

$C_{v,k}$  indicates the specific heat at constant volume. The former is called *criterion of thermal stability*, the latter *criterion of mechanical stability*. The criterion of thermal stability is generally satisfied by the EoS, however the respect of mechanical stability is not always ensured. Many EoS satisfy the mechanical stability until the so-called *spinodal line*, the line that separates the unstable domain from the stable/metastable one.

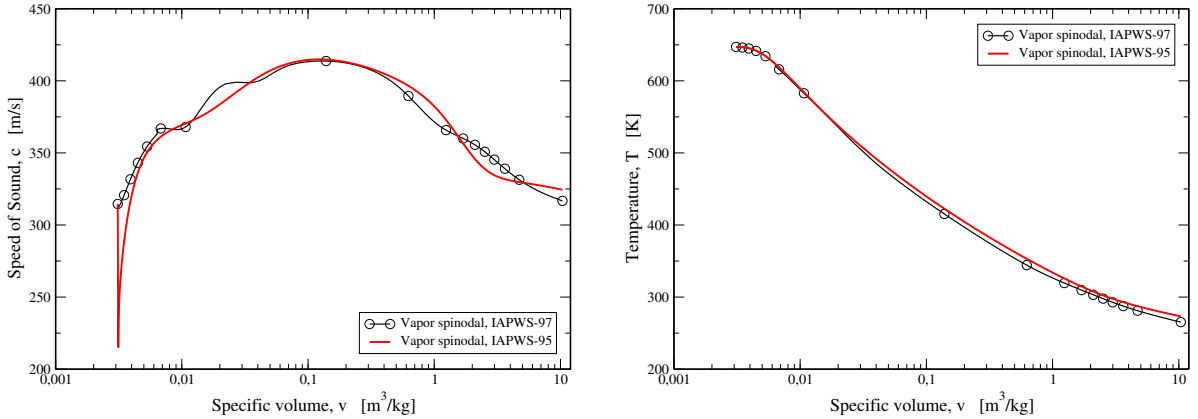


Figure 2: Speed of sound and temperature profiles on the vapor spinodal curve. The results obtained using the IAPWS-IF97 are compared to the ones obtained with the IAPWS-95.

To identify the domains where Eqs. 12 and 13 are physically defined, phasic spinodal curves must be identified. For the liquid spinodal curve, we rely on our previous work in [17] where we identified and compared it with results available in the literature. In [17] we defined the liquid domain limit as the composition of liquid spinodal and isobar  $p = 0$  curves. However, there are many references and measurements, which prove that the liquid can appear in metastable conditions at negative pressure (liquid under tension) also in the nuclear safety applications [28], therefore we expect to extend this tabulation to the negative pressure domain in the future.

The identification of the vapor spinodal curve is discussed in the next section.

### 3.2. Extension to vapor metastable states

In fast transients of nuclear industry concerns, one or both phases can be metastable. The liquid can reach metastable states due to a rapid depressurization (see [17] or Section 5), and the vapor can depart from equilibrium conditions during the vapor pocket compression initiating a waterhammer. But, metastable vapor is also of concern in the expansion stages of the steam turbines, both in nuclear and in conventional steam power plants.

For these reasons, the steam-water tables that we have proposed in [17] need to be extended to metastable vapor states. For prior works similar to the present one, refer to [34, 57]. In this section we provide a method of determination of the thermodynamical states belonging to the vapor spinodal curve, which allows us the extension to metastable vapor conditions included between the saturation curve and the spinodal one.

Contrary to what was done in [17] for the liquid spinodal curve, the properties of the vapor spinodal curve have been determined using the IAPWS-95 formulation. In fact, the IAPWS-95 expresses the thermodynamical variables as a function of  $v = 1/\rho$  and  $T$ , therefore, it exists a function of the form

$$p = p(v, T), \quad (16)$$

that allows one to define the loci at which

$$\left(\frac{\partial p}{\partial v}\right)_T = 0. \quad (17)$$

These correspond to the limit of thermodynamic stability for a pure phase, then they define the spinodal curve [7, 15]. As visible from Eqs. (10), IAPWS-IF97 can express a relation in the form of Eq. (16) in Region 3 only. For the liquid domain, in [17], we used the IAPWS-IF97 to define the spinodal curve because Region 3 almost entirely defines the metastable liquid domain. However, for the vapor phase it is not possible because the metastable vapor is only partially defined by Region 3 equation of state.

To overcome this difficulty, the vapor spinodal curve has been identified using the IAPWS-95. However, metastable vapor properties are everywhere defined using the IAPWS-IF97. Even on the vapor spinodal curve, once it has been identified by the IAPWS-95, thermodynamic properties are recalculated using the IAPWS-IF97 to guarantee thermodynamic properties continuity on the whole domain. In Fig. 2 we show the comparison between the pure vapor temperature and speed of sound on the vapor spinodal curves obtained by IAPWS-95 and IAPWS-IF97. The trends are very similar.

Once the vapor spinodal curve has been identified, the domain of the steam-water tables can be extended up to this limit. Beyond this limit, the fluid is unstable, then non physical. That is the reason why the spinodal lines represent an impassable boundary in our work.

### 3.3. The $e$ - $v$ diagram for water

The  $e$ - $v$  diagram is quite uncommon in the literature. The water phase diagram is clearly subdivided into three portions: liquid phase, vapor phase and unstable domain. To identify liquid and vapor phases on this diagram, refer to Fig. 3. The liquid region, located on the left of the  $e$ - $v$  diagram, is defined up to the critical point and up to the composition of liquid spinodal and isobar  $p = 0$ . The vapor domain is the one located above of the critical point and the vapor spinodal line.

The area comprised between the two spinodal lines is not of interest because it refers to phasic unstable states.

In [17] we have shown the behavior of thermodynamic properties in this plane, and the trend of isotherms, isobars and isoquality curves for single-phase water and mixtures at saturated conditions. Here, we make a different use of this diagram because we need one equation of state per phase. In Fig. 4 we show 2D trends of pressure, temperature and speed of sound on the whole  $e$ - $v$  domain. Note that the 2D plots here reported are intended for phasic liquid and vapor, in stable and metastable conditions, then, their behaviors beyond the saturation curve do not correspond to the mixture plots shown in [17].

### 3.4. A bicubic interpolation method

For the sake of simplicity, during the interpolation process, the irregular physical domain  $e$ - $v$ , has been transposed in a Cartesian transformed domain,  $Y$ - $X$ . This feature is depicted in Fig. 5 and exhaustively

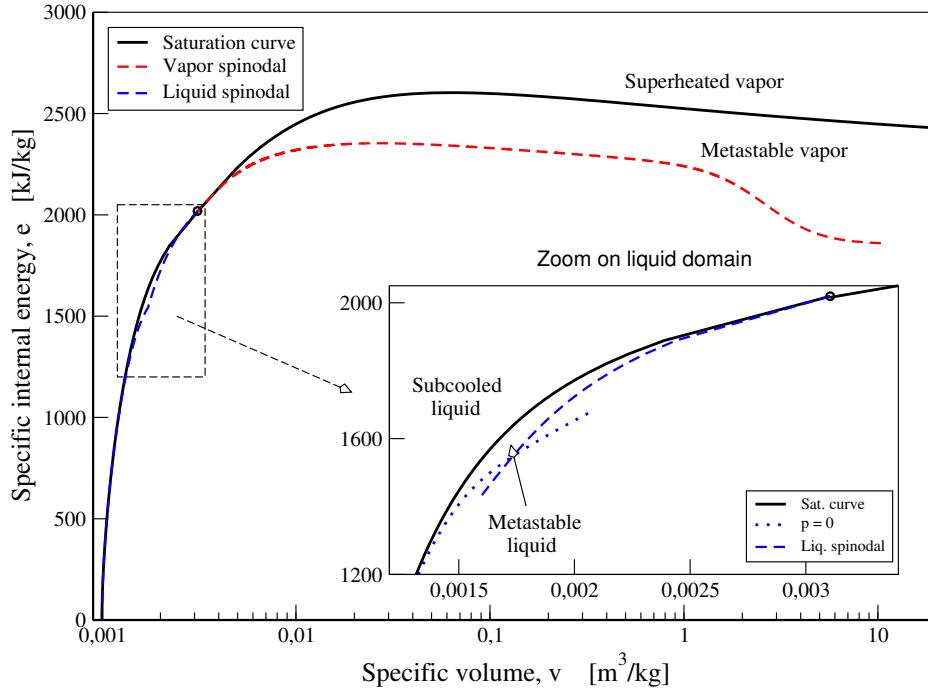


Figure 3: Liquid and vapor water on  $e$ - $v$  diagram. Critical point is indicated by circular markers  $\circ$  in both main plot and its magnified view. The black curve is the saturation curve, representing the loci at which phases are at saturated conditions. The red curve is the vapor spinodal, then, the region of metastable vapor is the one comprised between the saturation curve and the vapor spinodal. The blue curves represent the rightmost limit of the metastable liquid and is composed of two curves: the negative pressure border and the liquid spinodal. Thus, the metastable liquid is the narrow region comprised between the saturation curve and the blue lines. The wide region comprised between the two spinodals represents the unstable region, where a pure phase can not exist. This plot has been realized using both IAPWS-IF97 and IAPWS-95.

discussed in [33].

As previously done in [33], in the liquid and supercritical domain we imposed an equidistant pattern of nodes, hence the distribution is linear, whereas, in the vapor domain the node distribution is logarithmic. Handling such a regular distribution of nodes ensures that the cell containing the working point can be immediately found. Such a feature allows to strongly reduce the computational time for the cell identification. An alternative approach would be the one used in [22, 32], where the the physical domain was divided in an unstructured thermodynamic table.

Then, a *bicubic interpolation* is performed in the Cartesian diagram  $Y$ - $X$ , using stored values of  $e$ - $v$  diagram.

To perform a bicubic interpolation, the cell must be square. A *bilinear mapping* is used to pass from physical domain to Cartesian one. The bilinear mapping functions are:

$$v = \alpha_1 + \alpha_2 X + \alpha_3 Y + \alpha_4 XY, \quad (18)$$

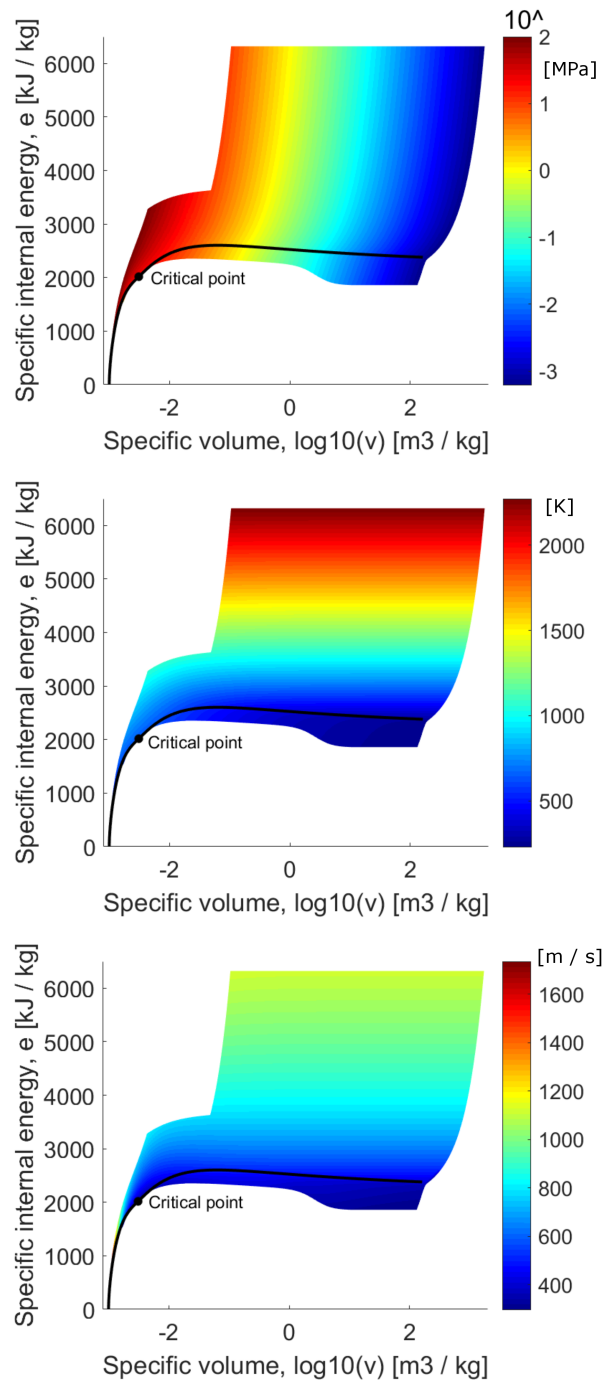


Figure 4: Phasic pressures (MPa), temperatures (K) and speeds of sound (m/s) on  $e$ - $v$  diagram. Results obtained using the IAPWS-IF97. The black line indicates the saturation curve. [The properties in the liquid domain are not clearly visible here. For a clearer representation of this domain, see \[17\].](#)

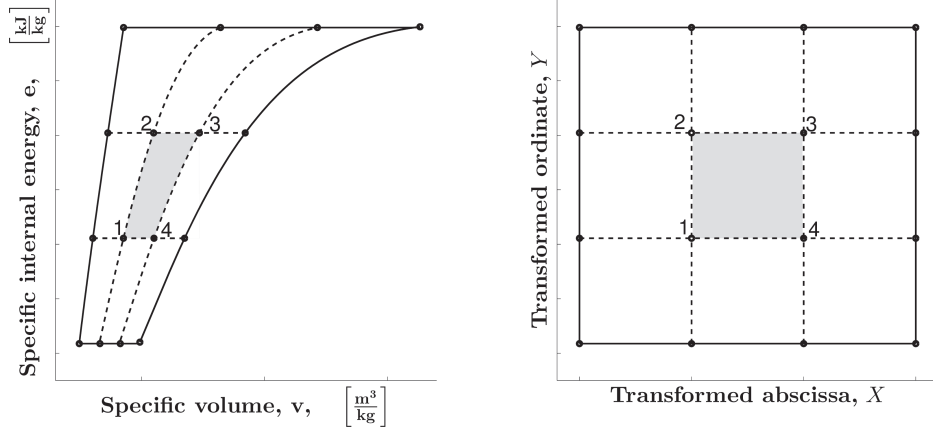


Figure 5: Grid of nodes in the physical domain and in the transformed one

and

$$e = \beta_1 + \beta_2 X + \beta_3 Y + \beta_4 XY. \quad (19)$$

To identify  $\alpha_i$ ,  $\beta_i$  coefficients, one needs to set the vertices of the irregular cell in the  $e$ - $v$  plane to be the vertices of the unit length square of the transformed space (see Fig. 5). In our particular case, the grid is formed by horizontal iso- $e$  lines, then:  $\beta_2, \beta_4 = 0$ . Finally, it comes out:

$$\alpha_1 = v_1, \quad \alpha_2 = -v_1 + v_4, \quad \alpha_3 = -v_1 + v_2, \quad \alpha_4 = v_1 - v_2 + v_3 - v_4, \quad (20)$$

$$\beta_1 = e_1, \quad \beta_2 = 0, \quad \beta_3 = -e_1 + e_2, \quad \beta_4 = 0. \quad (21)$$

The bilinear mapping serves to identify the  $(X_0, Y_0)$  point corresponding to a phasic  $(v_{k,0}, e_{k,0})$  value. Once the point is known, we can calculate the thermodynamic properties using a bicubic interpolation. Let us suppose to be interested in phasic pressure calculation, thus:

$$p_k(v_{k,0}, e_{k,0}) = \tilde{p}_k(X_0, Y_0) = [1 \ X_0 \ X_0^2 \ X_0^3] \mathbf{A} [1 \ Y_0 \ Y_0^2 \ Y_0^3]^T \quad (22)$$

where  $\mathbf{A}$  is the coefficient matrix describing the function  $p_k$  in the transformed space. Its elements are

$$\mathbf{A} = \begin{bmatrix} 1 & 0 & 0 & 0 \\ 0 & 0 & 1 & 0 \\ -3 & 3 & -2 & -1 \\ 2 & -2 & 1 & 1 \end{bmatrix} \begin{bmatrix} \tilde{p}_{k,1} & \tilde{p}_{k,2} & \partial_Y \tilde{p}_{k,1} & \partial_Y \tilde{p}_{k,2} \\ \tilde{p}_{k,4} & \tilde{p}_{k,3} & \partial_Y \tilde{p}_{k,4} & \partial_Y \tilde{p}_{k,3} \\ \partial_X \tilde{p}_{k,1} & \partial_X \tilde{p}_{k,2} & \partial_{X,Y} \tilde{p}_{k,1} & \partial_{X,Y} \tilde{p}_{k,2} \\ \partial_X \tilde{p}_{k,4} & \partial_X \tilde{p}_{k,3} & \partial_{X,Y} \tilde{p}_{k,4} & \partial_{X,Y} \tilde{p}_{k,3} \end{bmatrix} \begin{bmatrix} 1 & 0 & -3 & 2 \\ 0 & 0 & 3 & -2 \\ 0 & 1 & -2 & 1 \\ 0 & 0 & -1 & 1 \end{bmatrix}, \quad (23)$$

where, for instance,  $\partial_X \tilde{p}_{k,1}$  indicates the derivative of the function  $p_k$  with respect to the coordinate  $X$  at node 1, that is, the node in the bottom left corner. One can refer to [17] for further information about the calculations of these derivatives.

The function  $\tilde{p}_k(X, Y)$  refers to a Cartesian square grid and, by construction [41], has the following properties: i) values of the function and the specified derivatives are reproduced exactly at the nodes, and,



ii) the function and the specified derivatives change continuously across cell edges. Furthermore, these smoothness properties do not depend on the accuracy of the specified derivatives [41].

Similarly to phasic pressures, we have tabulated also phasic temperatures, sonic velocities and Gibbs free enthalpies to have a faster numerical method. Due to the choice of the bilinear transformation,  $p_k(v_k, e_k)$ ,  $T_k(v_k, e_k)$ ,  $c_k(v_k, e_k)$  and  $g_k(v_k, e_k)$  are globally continuous functions on the whole  $e$ - $v$  plan, but not all their derivatives are continuous across edges.

#### 4. Numerical solution methods

The numerical solution of system (6) can be obtained by a succession of operators [53] of first order,

$$\mathbf{U}_i^{n+1} = L_{source}^{\Delta t} L_{hyp}^{\Delta t} \mathbf{U}_i^n \quad (24)$$

or second order

$$\mathbf{U}_i^{n+1} = L_{source}^{\Delta t/2} L_{hyp}^{\Delta t} L_{source}^{\Delta t/2} \mathbf{U}_i^n, \quad (25)$$

where  $L_{hyp}$  and  $L_{source}$  denote, respectively, the hyperbolic and the source operator. The latter is composed by three operators:  $L_p$ ,  $L_T$ ,  $L_g$  that are, respectively, operators for pressure, temperature and chemical potential relaxation procedures. The result of an operator is used as initial value for the following operator.

The calculation variables vector, at the end of the hyperbolic operator step, will be called

$$\mathbf{U}_i^{n+} = L_{hyp}^{\Delta t} \mathbf{U}_i^n. \quad (26)$$

In this section, we describe the numerical techniques used for solving the hyperbolic homogeneous portion of the system and then relaxation operators.

##### 4.1. Hyperbolic operator

The hyperbolic homogeneous portion of the model, that is, Eq. (1), can be written as

$$\partial_t \mathbf{U} + \partial_z \mathbf{F}(\mathbf{U}) + \mathbf{B}_1(\mathbf{U}) \partial_z u + \mathbf{B}_2(\mathbf{U}) \partial_z(\alpha_1 p_1) + \mathbf{B}_3(\mathbf{U}) \partial_z(\alpha_2 p_2) = 0, \quad (27)$$

where:

$$\mathbf{U} = \begin{bmatrix} \alpha_1 \\ \alpha_1 \rho_1 \\ \alpha_2 \rho_2 \\ \rho u \\ \alpha_1 \rho_1 E_1 \\ \alpha_2 \rho_2 E_2 \end{bmatrix}, \quad \mathbf{F} = \begin{bmatrix} \alpha_1 u \\ \alpha_1 \rho_1 u \\ \alpha_2 \rho_2 u \\ \rho u^2 + \alpha_1 p_1 + \alpha_2 p_2 \\ \alpha_1 (\rho_1 E_1 + p_1) u \\ \alpha_2 (\rho_2 E_2 + p_2) u \end{bmatrix}, \quad \mathbf{B}_1 = \begin{bmatrix} -\alpha_1 \\ 0 \\ 0 \\ 0 \\ 0 \\ 0 \end{bmatrix}, \quad \mathbf{B}_2 = \begin{bmatrix} 0 \\ 0 \\ 0 \\ 0 \\ -u Y_2 \\ +u Y_2 \end{bmatrix}, \quad \mathbf{B}_3 = \begin{bmatrix} 0 \\ 0 \\ 0 \\ 0 \\ +u Y_1 \\ -u Y_1 \end{bmatrix}. \quad (28)$$

Considering a spatial domain decomposed in cells, we refer to  $\mathbf{U}_i^n$  as the integral average of the calculation variables vector in  $i$ th cell at time step  $t^n$ . The evolution between  $t^n$  and  $t^{n+}$  is

$$\mathbf{U}_i^{n+} = \mathbf{U}_i^n - \frac{\Delta t}{\Delta z} \left( \mathbf{F}_{i+\frac{1}{2}}^n - \mathbf{F}_{i-\frac{1}{2}}^n \right) - \Delta t H_i \quad (29)$$

where  $\mathbf{F}_{i\pm\frac{1}{2}}^n$  denotes the fluxes at mesh cell boundaries, and  $H_i$  groups all contributions of non-conservative terms, that is

$$H_i = \int_{\Delta z} \mathbf{B}_1 \partial_z u \, dz - \int_{\Delta z} \mathbf{B}_2 \partial_z (\alpha_1 p_1) \, dz - \int_{\Delta z} \mathbf{B}_3 \partial_z (\alpha_2 p_2) \, dz. \quad (30)$$

Equation (29) is exact, however we need an approximation method to evaluate both the fluxes and the integral of non-conservative terms. For the former we adopt a HLLC-type method, then the numerical approximation of the flux is:

$$\mathbf{F}_{i+\frac{1}{2}}^{HLLC,n}(\mathbf{U}_i^n, \mathbf{U}_{i+1}^n) = \begin{cases} \mathbf{F}_\ell, & \text{if } S_\ell > 0, \\ \mathbf{F}_\ell^* = \mathbf{F}_\ell + S_\ell(\mathbf{U}_\ell^* - \mathbf{U}_\ell), & \text{if } S_\ell \leq 0 < S^*, \\ \mathbf{F}_r^* = \mathbf{F}_r + S_r(\mathbf{U}_r^* - \mathbf{U}_r), & \text{if } S^* \leq 0 < S_r, \\ \mathbf{F}_r, & \text{if } S_r \leq 0. \end{cases} \quad (31)$$

This solver is *complete* because it assumes as many waves as the ones of the system. In fact, three waves are present and move at speeds

$$s^1 = S_\ell, \quad s^2 = S^*, \quad s^3 = S_r. \quad (32)$$

They separate four constant states called:  $\mathbf{U}_\ell$ ,  $\mathbf{U}_\ell^*$ ,  $\mathbf{U}_r^*$  and  $\mathbf{U}_r$ . We indicate with subscripts  $^*\ell$ ,  $^*r$  the quantities corresponding to the states  $\mathbf{U}_\ell^*$  and  $\mathbf{U}_r^*$  adjacent (respectively on the left and on the right) to the middle wave propagating at speed  $S^*$ . Following Davis [14] we define

$$S_\ell = \min(u_\ell - c_\ell, u_r - c_r), \quad S_r = \max(u_\ell + c_\ell, u_r + c_r). \quad (33)$$

The speed  $S^*$  is then determined as in [58]:

$$S^* = u^* = \frac{p_r - p_\ell + \rho_\ell u_\ell (S_\ell - u_\ell) - \rho_r u_r (S_r - u_r)}{\rho_\ell (S_\ell - u_\ell) - \rho_r (S_r - u_r)}. \quad (34)$$

The completely upwind fluxes of Eq. (31) are:  $\mathbf{F}_\ell = \mathbf{F}(\mathbf{U}_i^n)$  and  $\mathbf{F}_r = \mathbf{F}(\mathbf{U}_{i+1}^n)$ . The middle states are:

$$\mathbf{U}_\ell^* = \begin{bmatrix} \alpha_{1,\ell} \\ (\alpha_1 \rho_1)_\ell \frac{S_\ell - u_\ell}{S_\ell - S^*} \\ (\alpha_2 \rho_2)_\ell \frac{S_\ell - u_\ell}{S_\ell - S^*} \\ \rho_\ell \frac{S_\ell - u_\ell}{S_\ell - S^*} S^* \\ (\alpha_1 \rho_1)_\ell \frac{S_\ell - u_\ell}{S_\ell - S^*} \left( E_{1,\ell} + (S^* - u_\ell) \left( S^* + \frac{p_{1,\ell}}{\rho_{1,\ell} (S_\ell - u_\ell)} \right) \right) \\ (\alpha_2 \rho_2)_\ell \frac{S_\ell - u_\ell}{S_\ell - S^*} \left( E_{2,\ell} + (S^* - u_\ell) \left( S^* + \frac{p_{2,\ell}}{\rho_{2,\ell} (S_\ell - u_\ell)} \right) \right) \end{bmatrix}, \quad (35)$$

with  $\iota = \ell, r$ .

Non-conservative terms are approximated using a first order approximation method, that is

$$\int_{\Delta z} \mathbf{B}_1(U) \partial_z u \, dz \approx \mathbf{B}_1(U_i^n) (u_{i+\frac{1}{2}} - u_{i-\frac{1}{2}}), \quad (36)$$

$$\int_{\Delta z} \mathbf{B}_2(U) \partial_z(\alpha_1 p_1) \, dz \approx \mathbf{B}_1(U_i^n) [(\alpha_1 p_1)_{i+\frac{1}{2}} - (\alpha_1 p_1)_{i-\frac{1}{2}}], \quad (37)$$

$$\int_{\Delta z} \mathbf{B}_3(U) \partial_z(\alpha_2 p_2) \, dz \approx \mathbf{B}_1(U_i^n) [(\alpha_2 p_2)_{i+\frac{1}{2}} - (\alpha_2 p_2)_{i-\frac{1}{2}}]. \quad (38)$$

In order to calculate the interfacial quantities, we use the wave pattern information coming from the HLLC solver. For the advection equation we use the method proposed in [30]:

$$u_{i+\frac{1}{2}}^{HLLC,n}(\mathbf{U}_i^n, \mathbf{U}_{i+1}^n) = \begin{cases} u_\ell, & \text{if } S_\ell > 0, \\ \frac{S_\ell - u_\ell}{S_\ell - S^*} S^*, & \text{if } S_\ell \leq 0 < S^*, \\ \frac{S_r - u_r}{S_r - S^*} S^*, & \text{if } S^* \leq 0 < S_r, \\ u_r, & \text{if } S_r \leq 0. \end{cases} \quad (39)$$

For the non-conservative terms of the phasic energy equations, we propose:

$$(\alpha_k p_k)_{i+\frac{1}{2}}^{HLLC,n}(\mathbf{U}_i^n, \mathbf{U}_{i+1}^n) = \begin{cases} (\alpha_k p_k)_\ell, & \text{if } S_\ell > 0, \\ \alpha_{k,\ell} [p_{k,\ell} - \rho_{k,\ell} (S_\ell - u_\ell)(u_\ell - S^*)], & \text{if } S_\ell \leq 0 < S^*, \\ \alpha_{k,r} [p_{k,r} - \rho_{k,r} (S_r - u_r)(u_r - S^*)], & \text{if } S^* \leq 0 < S_r, \\ (\alpha_k p_k)_r, & \text{if } S_r \leq 0. \end{cases} \quad (40)$$

The hyperbolic operator just described has been intensively studied and tested in our previous works [18, 20]. In particular in [18] we compared various Riemann solvers for the six-equation system, assessing the performance of the solvers with mesh convergence tests and efficiency studies at first and second order. Moreover, we also studied the performance of different discretizations of the non-conservative terms in the energy equations and we investigated conditions leading to discrepancies with respect to the exact solution of the pressure equilibrium model based on the Rankine–Hugoniot conditions established in [48]. Difficulties related to non-conservative terms seem to arise only in the case of strong shocks in genuine two-phase mixture zones. Our numerical model therefore appears adequate for the applications to fast depressurizations of the present paper, which do not involve shock formation.

#### 4.2. Relaxation operators

In the literature, most of the works deal with instantaneous relaxation procedures to be used for very simple EoS as the stiffened gas one. In [19], the authors proposed novel techniques to describe the physics involved into the relaxation mechanisms. They consist of dynamical systems of ordinary differential equations

that allow the equilibrium recovery. The novelty of this work lies in the EoS independence of the numerical techniques.

These relaxation processes can be split into three systems of ODEs, each one modeling a different physical phenomenon. In this work the systems of ODEs are calculated using a high order explicit Runge-Kutta (RK) method with adaptive stepsize, that is, the so-called RK45 [26]. This method is fourth order accurate with an error estimator of fifth order for the calculation of the variable time step.

The drawback of this explicit method is the loss of stability for stiff problems. However, one may refer to the appendix of [19] for alternative robust semi-analytical methods if needed.

At the end of the hyperbolic operator step, phases are in full thermodynamic disequilibrium. This is reduced using three relaxation operators that are used in series. First the pressure equilibrium step, then the temperature relaxation one and, finally, the mass transfer procedure.

#### 4.2.1. Pressure relaxation operator

The pressure relaxation procedure is a system of ODEs composed of two equations. In the canonical form it writes

$$\begin{cases} \frac{d\rho_1}{dt} = -\frac{1}{a} \frac{p_1 - p_2}{\Theta^P}, \\ \frac{de_1}{dt} = -\frac{p_{int}}{a\rho_1^2} \frac{p_1 - p_2}{\Theta^P}, \end{cases} \quad (41)$$

where

$$a = \rho_1 \Gamma_1 \left[ \frac{p_{int}}{\rho_1^2} - \left( \frac{\partial e_1}{\partial \rho_1} \right)_{p_1} \right] + \rho_2 \Gamma_2 \frac{\alpha_1 \rho_2}{\alpha_2 \rho_1} \left[ \frac{p_{int}}{\rho_2^2} - \left( \frac{\partial e_2}{\partial \rho_2} \right)_{p_2} \right]. \quad (42)$$

$p_{int}$  indicates the interfacial pressure. [To see the consistency between System \(41\) and the corresponding first term in the right-hand-side of advection and energy equations in Eq. \(6\), refer to \[19\].](#) This relaxation is based on the first law of the thermodynamics and an exponential time-decay for the pressure disequilibrium. It allows a semi-analytical integration, then, it is very robust even for stiff cases ( $\Theta^P \ll 1$ ).

Since we use the six-equation model to integrate more easily the five-equation model of [31], the pressures equilibrium is required at the end of this pressure relaxation step. Hence, sufficiently small  $\Theta^P$  must be used. For instance, for  $\Theta^P = \Delta t^{conv}/9$ , the final pressure disequilibrium is around the 0.01% of the initial one. As a result, phases may be considered to be roughly in pressure equilibrium.

#### 4.2.2. Temperature relaxation operator

The temperature relaxation procedure is based on the first law of thermodynamics and the Newton's law for the convection. This step is the one responsible for the sensible heat transfer. In the canonical form, the system to solve is

$$\begin{cases} \frac{d\rho_1}{dt} = -\frac{hA_{int}}{V} (T_2 - T_1) \frac{1}{a} \left( \frac{\Gamma_1}{\alpha_1} + \frac{\Gamma_2}{\alpha_2} \right), \\ \frac{de_1}{dt} = -\frac{hA_{int}}{V} (T_2 - T_1) \left[ \frac{p_{int}}{a\rho_1^2} \left( \frac{\Gamma_1}{\alpha_1} + \frac{\Gamma_2}{\alpha_2} \right) - \frac{1}{m_1} \right]. \end{cases} \quad (43)$$

$h$  is the heat transfer coefficient expressed in  $W/m^2 \cdot K$  and  $A_{int}$  is the interface area expressed in  $m^2$  and flow pattern dependent. One can use some empirical correlations to estimate them or can use  $\frac{hA_{int}}{V}$  as a parameter for speeding up or slowing down the sensible heat transfer process.

To see the consistency between System (43) and the corresponding second term in the right-hand-side of advection and energy equations in Eq. (6), refer to [19].

For very fast temperature relaxation processes, a more robust technique is reported in the appendix of [19]. It is a semi-analytical procedure based on an exponential time-decay for the temperature disequilibrium.

#### 4.2.3. Mass transfer operator

The mass transfer procedure models the condensation and evaporation events. The procedure proposed in [19] is very flexible because it may incorporate various models present in the literature. For instance nucleation models (see [40, 42]), statistical mechanics theory (see [62]), or simpler relaxation models [5].

It is based on the pressure equilibrium between phases and phasic temperature difference invariance. This latter condition means that the heat transfer occurring in this processes is the latent one. No sensible heat transfer occurs. The canonical form of this relaxation process is

$$\begin{cases} \frac{dm_1}{dt} = -G_{1 \rightarrow 2} \frac{A_{int}}{V}, \\ \frac{d\rho_1}{dt} = -G_{1 \rightarrow 2} \frac{A_{int}}{V} \frac{i_p k_T - k_p i_T}{k_p j_T - j_p k_T}, \\ \frac{de_1}{dt} = -G_{1 \rightarrow 2} \frac{A_{int}}{V} \frac{j_p i_T - i_p j_T}{k_p j_T - j_p k_T}. \end{cases} \quad (44)$$

To close the system, a closure law for the mass transfer term  $G_{1 \rightarrow 2} A_{int}$  is needed.

The mass transfer is due to a chemical disequilibrium, that is, a difference between phasic Gibbs free enthalpies. For this reason, many authors in the literature assumes [36, 38, 39, 49, 64]:

$$G_{1 \rightarrow 2} \propto (g_1 - g_2). \quad (45)$$

In this work, we assume

$$G_{1 \rightarrow 2} \frac{A_{int}}{V} = \frac{g_1 - g_2}{\Theta_g}, \quad (46)$$

where  $\Theta_g$  is the characteristic time for the chemical equilibrium recovery. Such magnitude is not clearly known, then, we adopt a correlation inspired from [5, 17, 21], i.e.

$$\Theta_g = K_g \alpha_v^{-0.25} \left( \frac{p_{sat} - p}{p_{crit} - p_{sat}} \right)^{-1.8}, \quad (47)$$

where  $p_{sat}$  indicates the saturation pressure corresponding to the equilibrium temperature that has been already reached in the previous relaxation step. In case the thermal equilibrium has not been reached yet, it refers to the liquid temperature because in a depressurization the phenomenon that triggers the vaporization is the metastability of the liquid.

This term is fundamental because it controls the phase transition kinetics. It is important to precise that if the kinetics is not sufficiently fast, phases can go into a too deep metastability and, as a result, cross the spinodal line. When this occurs, the numerical simulation stops because an unstable thermodynamic state has been detected. Due to the proximity of the saturation line to the spinodal line, the detection of unphysical states is more likely to occur for the liquid phase than for the vapor one (see Fig. 3).

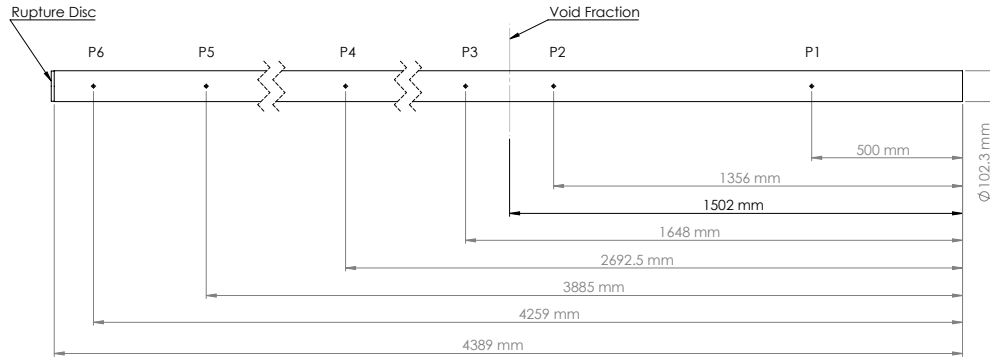


Figure 6: Schematic of Super Canon experimental facility and location of the measurement devices.

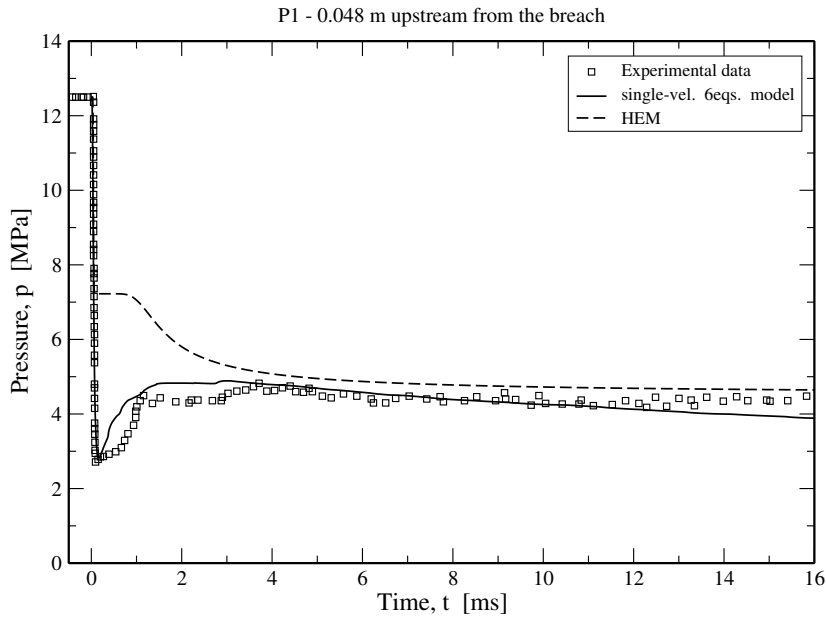


Figure 7: Pressure evolution in the first 16 ms of the Bartak's experiment [3] (12.5 MPa, 563.15 K). Assessment of the single-velocity six-equation model against the experimental data and the HEM results. For this calculation, the 1.7 m long tube has been discretized into a 1000 cells mesh and  $K_g = 4$ .

## 5. Numerical simulations of fast depressurizations

In the context of nuclear safety, the Loss of Coolant Accident (LOCA) is one of the Design Basis Accidents (DBA). It represents the sudden rupture of a primary system pipe of a nuclear power plant. When it occurs, a rarefaction wave originates at the breach and moves upstream in the primary circuit. The interaction of this wave with the reactor core may lead to the mechanical damage of core components. Then, for the fluid-structure analysis, the correct calculation of the rarefaction wave amplitude is of paramount importance.

The thermodynamic disequilibrium plays a crucial role on the rarefaction wave amplitude, thus, a simple HEM can not produce a correct simulation of these flows. Therefore, to improve the industrial simulation tools, the single-velocity six-equation model has been implemented in the fast dynamic code EUROPLEXUS.

Since the phenomena involving metastable states were not completely known, in the '70s-'80s, some experimental campaigns have been carried out. The experimental facilities for the industrial scenarios focused on the rapid depressurization of vessels or pipes containing water at subcooled conditions [3, 23, 45].

In this section we use these experiments for the validation of the methodology discussed above with the EUROPLEXUS code. The benchmark is performed using the experimental data of Bartak [3], Edwards-O'Brien [23] and Super Canon test rig [45].

### 5.1. *Experimental device description*

Super Canon facility was set up in France in the '70s and its experimental campaign was more devoted to the global transient, that is, for the analysis of the two-phase flow features from the break up to the complete blown down of the test rig. The schematic of the Super Canon facility and the measurement devices are shown in Fig. 6. It consists in a 4.389 m long horizontal pipe, with an internal diameter of 102.3 mm completely filled with degassed water. At one extremity of the pipe, there is a rupture disc whose sudden opening triggers the pipe depressurization. The opening is the 100% of the cross section. At the other extremity, the pipe is fully closed. It comprises six pressure transmitters and a void fraction measurement device.

The Edwards-O'Brien test rig is similar to the Super Canon one. It is an horizontal pipe of 4.096 m with an internal diameter of 73.15 mm. Unlike the previous experiments, the cross section of the break is 12.5% smaller than the cross section of the pipe.

Conversely to the previous ones, the Bartak test rig consists of a pressure vessel and a discharge pipe of 1.7 m equipped with pressure transmitters and a rupture disc at the end. The internal diameter of the discharge pipe is 80 mm and the abrupt opening is the 100% of the cross section.

For further details about the test rig geometries and the measurement techniques, one may refer to [3, 23, 45].

For all tests, the fluid is at rest at the moment of the abrupt opening. The initial pressure and temperature conditions are  $12.5 \text{ MPa}$  and  $563.15 \text{ K}$  for the Bartak test,  $10.34 \text{ MPa}$  and  $557.59 \text{ K}$  for the Edwards-O'Brien test, and  $15 \text{ MPa}$  and  $593.15 \text{ K}$  for the Super Canon test. Then, the corresponding subcooling degrees, i.e.  $T_{sat}(p_{in}) - T_{in}$ , are, respectively,  $38 \text{ K}$ ,  $29 \text{ K}$  and  $22 \text{ K}$ . Generally, the higher the subcooling degree, the deeper the metastability reached.

All numerical tests have been simulated using a simplified 1D geometry. The sudden opening is simulated as a Riemann problem with the experimental conditions on one side of the discontinuity and a quasi-infinite vessel filled atmospheric steam on the other side. On the end of the pipe, for Super Canon and Edwards-O'Brien tests, there is a wall boundary conditions. Whereas, for Bartak test, the pressure vessel is modeled as a 0D vessel of large dimensions.

For all tests, we conducted a convergence study and we report here only the results obtained using a 1000 cells mesh. These results are no longer affected by nodalization choices.

## 5.2. Analysis of the numerical results

At that moment, a rarefaction wave originates at the break and moves backward. The very first part of the transient is well represented by the Bartak and Edwards-O'Brien data, whereas, the Super Canon experiments represent the global transient.

The depressurization is initially abrupt and fast, then pressure drops below the saturation pressure corresponding to the initial stagnation temperature ( $7.4 \text{ MPa}$  in Bartak experiment,  $6.8 \text{ MPa}$  in Edwards-O'Brien test,  $11.2 \text{ MPa}$  for Super Canon). The liquid water is then into the metastable domain.

Since the abrupt depressurization has led the liquid into a deep metastable condition, the fluid is driven from the thermo-chemical disequilibrium towards the thermodynamic stability condition. Then, the depressurization is stopped by a quick vaporization, also called explosion-like nucleation. The system pressure is therefore driven towards the saturated conditions. Further discussions about the rate of depressurization, the pressure undershoot and the homogeneous nucleation phenomenon can be found in [1, 3, 7, 15, 52].

In Fig. 7, 8, 9 and 10 we show the comparisons of the numerical simulations obtained with the single-velocity six-equation model and the experimental data. To underline the importance of the thermo-chemical disequilibrium, we report as well the numerical results of the HEM. From these figures we can observe that the pressure undershoot just discussed is well reproduced by the six-equation model, whereas, for the HEM, the mixture always remains at saturated conditions. This means that a numerical simulation performed with a HEM leads to an underestimation of the amplitude of the rarefaction wave, then, for a fluid-structure interaction analysis, the HEM leads to an underestimation of the mechanical consequences on the structure.

By the experimental measurements we know that the velocity of propagation of the rarefaction wave compares well with the isentropic speed of sound of the liquid water initially present into the system. From



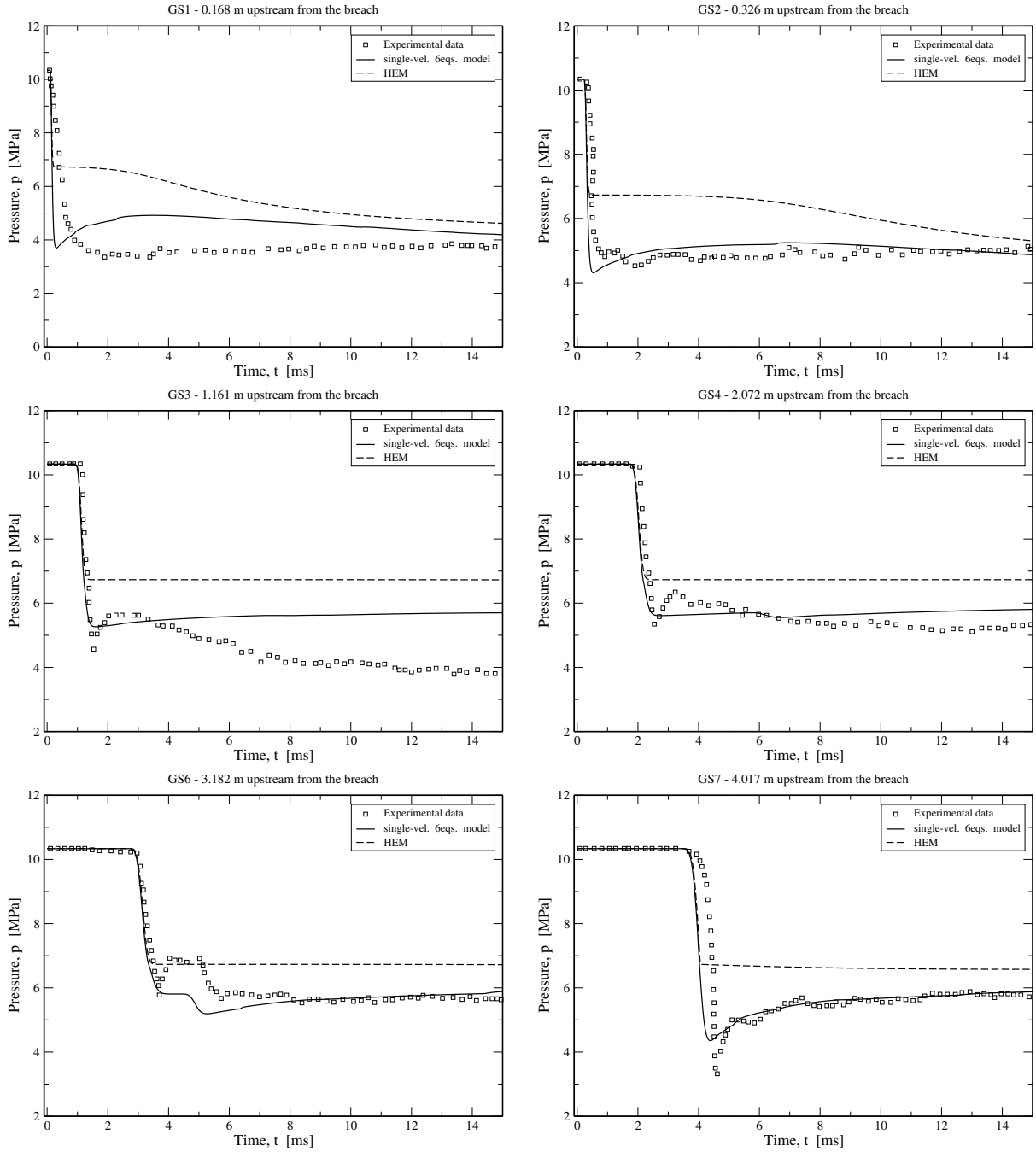


Figure 8: Assessment of the single-velocity six-equation model on a Edwards-O'Brien experiment. The initial stagnation conditions are  $10.34 \text{ MPa}$  and  $557.59 \text{ K}$  ( $1500 \text{ psia}$ ,  $544^\circ \text{ F}$ ). For this calculation, the  $4.096 \text{ m}$  long tube has been discretized into a 1000 cells mesh and  $K_g = 0.5$ .

Fig. 7, 8 we can see that this velocity is correctly simulated by both equilibrium and disequilibrium two-phase flow models.

For a HEM simulation, once the rarefaction wave has taken the fluid into the two-phase domain, phase

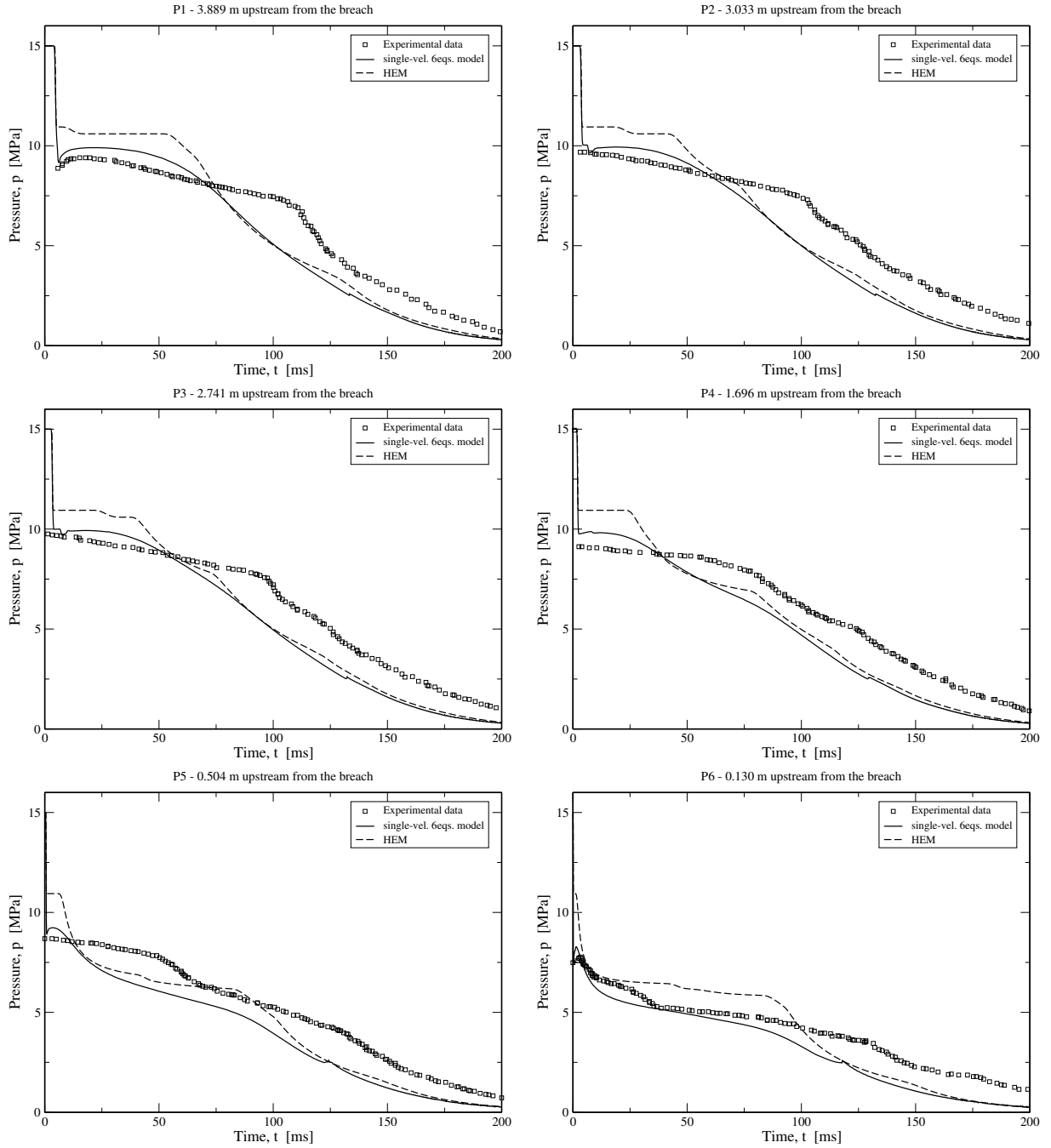


Figure 9: Assessment of the single-velocity six-equation model on a Super Canon experiment: pressure evolution. The initial stagnation conditions are 15 MPa and 593.15 K. For this calculation, the 4.389 m long tube has been discretized into a 1000 cells mesh and  $K_g = 0.6$ .

transition takes place in order to maintain phases at full thermodynamic equilibrium. In this case, phase transition starts when the fluid reaches the saturated liquid curve.

For the single-velocity six-equation model, the rarefaction wave propagates into the liquid and takes

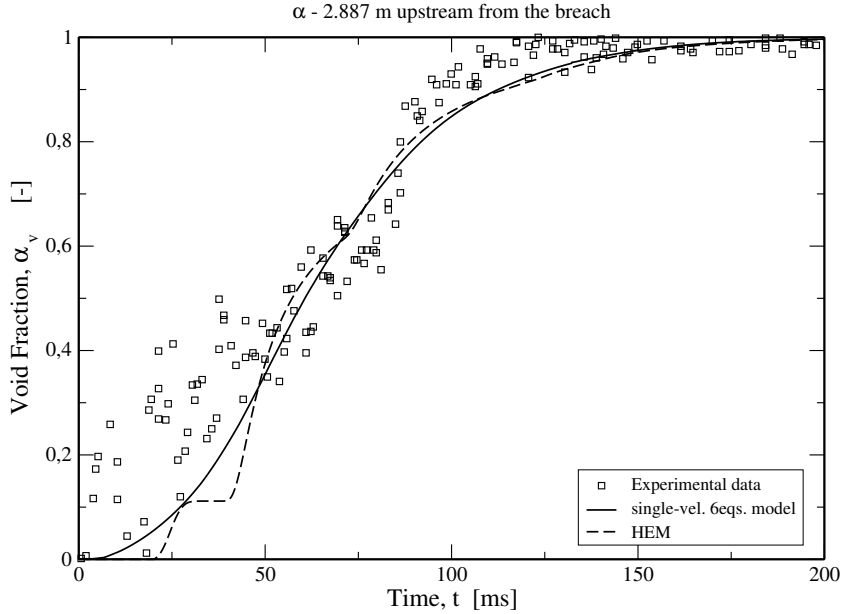


Figure 10: Assessment of the single-velocity six-equation model on a Super Canon experiment: void fraction evolution. The initial stagnation conditions are 15 MPa and 593.15 K. For this calculation, the 4.389 m long tube has been discretized into a 1000 cells mesh and  $K_g = 0.6$ .

it to metastable conditions. Phase transition does not take place immediately when the fluid reaches the saturated conditions, thus, the amplitude of the rarefaction wave is wider than in the HEM calculations. For the single-velocity six-equation model, the mass transfer that transforms the liquid into vapor is activated only when metastable conditions are detected. Once one of the two phases crosses the saturation curve, the mass transfer is activated and its intensity is proportional to the chemical disequilibrium (see Eq. (46)). This is coherent with the theory of thermodynamic stability according to which a deeper metastability condition leads to a faster mass transfer [7]. Summarizing, this modeling choice allows to well represent the two main physical features occurring in fast depressurizations: (i) the correct amplitude of the rarefaction wave, and (ii) the explosion-like nucleation phenomenon.

Considering the whole depressurization Super Canon experiment in Fig. 9, after the explosion-like nucleation at the first milliseconds, the pressure remains constant, but at values lower than the saturation one. Hence the liquid is still in metastable conditions. After 50 ms, the pressure decreases due to the emptying of the capacity. The emptying rate is imposed by the two-phase critical flow that sets at the breach [16].

## 6. Conclusions

In the present work we have developed a single-velocity six-equation model for phase transition flows, and implemented it in the EUROPLEXUS code. The industrial objective of this work was to provide the EUROPLEXUS code with a single-velocity hyperbolic model able to deal with thermal and chemical

disequilibria to be used for the fluid-structure interaction analysis of hypothetical accidents in nuclear reactors.

This work results from the merging of two techniques previously developed by the same authors. The first technique was the fast and accurate calculation of steam-water properties [17]. The second technique was the treatment of the relaxation processes source terms by means of EoS-independent numerical procedures [19].

Typically, one can distinguish two kinds of two-phase flow modeling approaches: an industrial one and an academical one. For the industrial-aimed numerical modeling, the process of equilibrium recovery between liquid and vapor is usually treated by using experimental correlations or simple models [4, 27, 43, 55]. The advantage of the industrial codes came from the capability to use accurate EoS or tabulated ones. In the academical numerical modeling context, the process of equilibrium recovery is often decomposed according to the physical disequilibria [11, 38, 49, 64]. Then, it is closer to the physics. However, the drawback of these procedures lies in the difficulty of using accurate EoS.

Nevertheless, for a wide industrial use, adopting accurate EoS is necessary. Our work is based on a physically consistent analysis of the metastable flows, that is widely used in the literature [11, 38, 49, 50, 64]. Thanks to that, the disequilibrium between the phases can be correctly taken into account because of the splitting of pressure, temperature and Gibbs free enthalpy disequilibria, and, at the same time, the numerical calculations rely on fast and accurate EoS.

The new methodology has been validated on experimental data of rapid depressurization tests available in the literature.

The perspectives of this work are multiple. From the industrial point of view, a medium-term perspective could be the adjustment of the relaxation techniques to the velocity disequilibrium case and their coupling with the seven-equation model already present in EUROPLEXUS [11, 37]. In that case, no adjustments would be necessary for using the steam-water tables within the seven-equation model.

From the academical point of view, thanks to the decoupling of the physical phenomena effects (compression, sensible heat and latent heat transfers), one can conduct a finer analysis of equilibrium recovery mechanisms. Using these techniques, it could be possible to increment the physical understanding of some phenomena, simulating vapor bubbles cavitation or liquid droplets vaporizations. This analysis of the thermal and chemical disequilibria can be useful to extrapolate new macroscopic correlations, for example. A preliminary step towards this goal has already started at *IMSIA*, joint laboratory EDF-CNRS-ENSTA-CEA. The single-velocity six-equation model together with the steam-water tables have been implemented on the high-order code called *Code\_Safari* [13, 24].

From the macroscopic point of view, the novel relaxation procedures allow to study some physical phenomena at different flow pattern regimes. It could be interesting to study the dependency of some phenomena on the topological magnitudes (interfacial area).

Moreover, the mass transfer procedure proposed in [19] and described in Section 4.2.3 allows us to take

into account different phase transition models using the same numerical framework. This could be used to conduct benchmark tests of the different phase transition models (nucleation models, relaxations models, etc.) against experimental data.

Lastly, despite our efforts, the irreversibility of the model has not been formally proven yet. Therefore, a perspective work is also the proof that the final model generates entropy in each of its interphase transfer terms.

## 7. Acknowledgments

The authors would like to gratefully thank Pascal Galon (CEA) and Frédéric Daude (EDF) for helpful discussions and advice for the implementation of the flow model in EUROPLEXUS.

## Appendix A. Coefficients for the mass transfer mechanism

The coefficient for the mass transfer process involve the partial derivatives of the thermodynamic properties and are:

$$\begin{aligned} i_p &= \rho_2 \Gamma_2 \frac{e_1 - e_2}{m_2} + \left( \frac{\partial p_2}{\partial \rho_2} \right)_{e_2} \frac{\rho_1 - \rho_2}{\alpha_2 \rho_1}, \\ j_p &= \left( \frac{\partial p_1}{\partial \rho_1} \right)_{e_1} + \left( \frac{\partial p_2}{\partial \rho_2} \right)_{e_2} \frac{\alpha_1 \rho_2}{\alpha_2 \rho_1}, \\ k_p &= \rho_1 \Gamma_1 + \rho_2 \Gamma_2 \frac{m_1}{m_2}, \end{aligned} \tag{A.1}$$

and

$$\begin{aligned} i_T &= \frac{1}{C_{v,2}} \frac{e_1 - e_2}{m_2} + \left( \frac{\partial T_2}{\partial \rho_2} \right)_{e_2} \frac{\rho_1 - \rho_2}{\alpha_2 \rho_1}, \\ j_T &= \left( \frac{\partial T_1}{\partial \rho_1} \right)_{e_1} + \left( \frac{\partial T_2}{\partial \rho_2} \right)_{e_2} \frac{\alpha_1 \rho_2}{\alpha_2 \rho_1}, \\ k_T &= \frac{1}{C_{v,1}} + \frac{1}{C_{v,2}} \frac{m_1}{m_2}. \end{aligned} \tag{A.2}$$

where  $\Gamma_k$  are the phasic Grüneisen coefficients,  $C_{v,k}$  are the phasic specific heats at constant volume and  $m_k = \alpha_k \rho_k$  are the phasic partial densities.

## Appendix B. Entropy source terms of the complete model

The interphasic processes are irreversible, then, they lead to an increase of the mixture entropy. To check this physical and mathematical feature, we now transform the energy source terms into corresponding entropy source terms. For this purpose, we use the product rules for derivatives and the fundamental thermodynamic differential

$$de_k = T_k ds_k + \frac{p_k}{\rho_k} d\rho_k. \tag{B.1}$$

Ignoring transport effects in Eq. (6), phasic entropies evolutions read:

$$\frac{ds_1}{dt} = \frac{(p_1 - p_{int})(p_1 - p_2)}{aT_1\rho_1^2\Theta_p}. \quad (\text{B.2a})$$

$$\frac{ds_2}{dt} = \frac{(p_{int} - p_2)(p_1 - p_2)}{aT_2\rho_1\rho_2\Theta_p} \frac{\alpha_1}{\alpha_2}. \quad (\text{B.2b})$$

Thus, considering that the mixture entropy is  $S = \alpha_1\rho_1s_1 + \alpha_2\rho_2s_2$ , its time-derivative is

$$\frac{dS}{dt} = -\frac{\alpha_1(p_1 - p_2)}{aT_1T_2\rho_1\Theta_p} [p_{int}(T_2 - T_1) + T_1p_2 - T_2p_1]. \quad (\text{B.3})$$

For the temperature relaxation process, the time evolutions of phasic entropies are

$$\frac{ds_1}{dt} = \frac{1}{\rho_1T_1} \frac{hA_{int}}{V} (T_2 - T_1) \left[ \frac{1}{a\rho_1} \left( \frac{\Gamma_1}{\alpha_1} + \frac{\Gamma_2}{\alpha_2} \right) (p_1 - p_{int}) + \frac{1}{\alpha_1} \right], \quad (\text{B.4a})$$

$$\frac{ds_2}{dt} = \frac{1}{\rho_2T_2} \frac{hA_{int}}{V} (T_2 - T_1) \left[ \frac{1}{a\rho_1} \left( \frac{\Gamma_1}{\alpha_1} + \frac{\Gamma_2}{\alpha_2} \right) (p_{int} - p_2) - \frac{1}{\alpha_1} \right] \frac{\alpha_1}{\alpha_2}. \quad (\text{B.4b})$$

The time-derivative of the mixture entropy is

$$\frac{dS}{dt} = \alpha_1 \frac{hA_{int}}{V} (T_2 - T_1) \left[ \frac{1}{a\rho_1} \left( \frac{\Gamma_1}{\alpha_1} + \frac{\Gamma_2}{\alpha_2} \right) \left( \frac{p_1 - p_{int}}{T_1} + \frac{p_{int} - p_2}{T_2} \right) + \frac{1}{\alpha_1} \left( \frac{1}{T_1} - \frac{1}{T_2} \right) \right]. \quad (\text{B.5})$$

For the general case of  $p_1 \neq p_2$ , investigating the sign of this function, it is too complex to analytically demonstrate the irreversibility of the process. In the limit case of  $p_1 = p_2$ , (B.5) becomes

$$\frac{dS}{dt} = \frac{hA_{int}}{V} \frac{(T_1 - T_2)^2}{T_1T_2} \geq 0. \quad (\text{B.6})$$

Hence, if the temperature relaxation occurs when phases are at pressure equilibrium, the sensible heat transfer process is irreversible as it must be. In our case, we have a stiff pressure relaxation forcing phasic pressures to numerically converge prior to proceeding with the temperature relaxation process. Therefore, we are very close to the limit case reported in (B.6).

Even if the thermal relaxation process occurs keeping  $p_1 \approx p_2$ , in order to check the physical consistency of our code, we calculate the mixture entropy at the beginning and at the end of this relaxation to notify whether it has decreased. In all the numerical tests performed so far, we have never detected a single decrease of the mixture entropy.

Finally, for the mass transfer process, the time-derivatives of phasic entropies are:

$$\frac{ds_1}{dt} = + \frac{\frac{p_1}{\rho_1^2}(i_p k_T - k_p i_T) - (j_p i_T - i_p j_T)}{(k_p j_T - j_p k_T)T_1} G_{1 \rightarrow 2} \frac{A_{int}}{V}, \quad (\text{B.7a})$$

$$\frac{ds_2}{dt} = - \frac{\frac{p_2}{\rho_1^2}(i_p k_T - k_p i_T) - (j_p i_T - i_p j_T)}{(k_p j_T - j_p k_T)T_2} G_{1 \rightarrow 2} \frac{A_{int}}{V} \frac{m_1}{m_2}, \quad (\text{B.7b})$$

for the mixture:

$$\frac{dS}{dt} = - \left[ \alpha_1 \rho_1 \frac{(T_1 - T_2)}{T_1 T_2} \frac{\frac{p_1}{\rho_1^2}(i_p k_T - k_p i_T) - (j_p i_T - i_p j_T)}{(k_p j_T - j_p k_T)} + (s_1 - s_2) \right] G_{1 \rightarrow 2} \frac{A_{int}}{V}. \quad (\text{B.8})$$

Similarly to temperature relaxation, it is too complex to analytically demonstrate the irreversibility of the process. But unlike temperature relaxation, it is not possible to define a limit case in which the irreversibility is ensured. To check the physical consistency of our code, we compute the mixture entropy at the beginning and at the end of the mass transfer process. In all the numerical tests performed so far, we have never detected a decrease of the mixture entropy. This empirical check is not to be intended as a proof of irreversibility, because it is just an informatic warning to notify whether the mixture entropy has ever decreased.

## References

- [1] Alamgir M., Lienhard J.H., 1981, Correlation of pressure undershoot during hot water depressurization. *J. Heat Transfer*, Vol. 103, 52-55.
- [2] Baer M.R., Nunziato J.W., 1986, A two-phase mixture theory for the deflagration-to-detonation transition (ddt) in reactive granular materials. *Int. J. Multiphase Flow*, Vol. 12, 861-89.
- [3] Bartak J., 1990, A study of the rapid depressurization of hot water and the dynamics of vapour bubble generation in superheated water. *Int. J. Multiphase Flow*, Vol. 16, 789-98.
- [4] Bestion D., 1990, The physical closure laws in the CATHARE code. *NED*, 124, 229-245.
- [5] Bilicki Z., Kestin J., 1990, Physical aspects of the relaxation model in two-phase flow, *Proceedings of the Royal Society A, Math. Phy. Sciences*, Vol. 428, 379-97.
- [6] Bilicki Z., Kestin J., Pratt M.M., 1990, A reinterpretation of the results of the Moby Dick experiments in terms on the nonequilibrium model, *ASME J. Fluids Engineering*, Vol. 112, 212-17.
- [7] Carey V.P., *Liquid-Vapor Phase-Change Phenomena*. Francis & Taylor, New York, USA.
- [8] Chiapolino A., Boivin P., Saurel R., 2017, A simple phase transition relaxation solver for liquid-vapor flows. *Int. J. Numer. Meth. Fluids* 2017; 83:583-605.
- [9] Coquel F., Gallouet T., Herard J.-M., and Seguin N., 2002, Closure laws for a two-fluid two-pressure model. *Comptes Rendus Mathematique*, Vol. 334, 927-32.
- [10] Cowperthwaite M., 1969, Relationships between Incomplete Equations of State, *J. Franklin Institute*, Vol. 285, 379-87.
- [11] Crouzet F., Daude F., Galon P., Hérard J.-M., Hurisse O., Liu Y., 2015, Validation of a two-fluid model on unsteady liquid-vapor water flows. *Computers & Fluids*, 119, 131-42.
- [12] Daude F., Galon P., Gao Z., Blaud E., 2014, Numerical experiments using a HLLC-type scheme with ALE formulation for compressible two-phase flows five-equation models with phase transition. *Comput. Fluids*, Vol. 94, 112-38.
- [13] Daude F., Berland J., Emmert T., Lafon Ph., Crouzet F., Bailly C., 2012, A high-order finite-difference algorithm for direct computation of aerodynamic sound. *Comput. Fluids*, Vol. 61, 46-63.
- [14] Davis S.F., 1988, Simplified second-order Godunov-type methods. *SIAM J. Sci. Stat. Comput.*, Vol. 9, 445-73.
- [15] Debenedetti P.G., 1996, *Metastable Liquids: Concepts and Principles*. Princeton University Press, Princeton, NJ.
- [16] De Lorenzo M., Lafon Ph., Seynhaeve J.-M., Bartosiewicz Y., 2017, Benchmark of Delayed Equilibrium Model (DEM) and Classic Two-Phase Critical Flow Models against Experimental Data. *Int. J. Multiphase Flow*, Vol. 92, 112-30.
- [17] De Lorenzo M., Lafon Ph., Di Matteo M., Pelanti M., Seynhaeve J.-M., Bartosiewicz Y., 2017, Homogeneous Two-Phase Flow Models and Accurate Steam-Water Table Look-up Method for Fast Transient Simulations. *Int. J. Multiphase Flow*, Vol. 95, 199-219.
- [18] De Lorenzo M., Pelanti M., Lafon Ph., 2018, HLLC-type and path-conservative schemes for a single-velocity six-equation two-phase flow model: a comparative study. *Applied Mathematics and Computation*, Vol. 333C, 95-117.

- [19] De Lorenzo M., Lafon Ph., Pelanti M., 2019, A hyperbolic phase-transition model with non-instantaneous EoS-independent relaxation procedures. *J. Comput. Phys.*, Vol. 379, 279-308.
- [20] De Lorenzo M., 2018, Modelling and numerical simulation of metastable two-phase flows. Ph.D. thesis from Université Paris-Saclay.
- [21] Downar-Zapolski P., Bilicki Z., Bolle L., Franco J., 1996, The non-equilibrium relaxation model for one-dimensional flashing liquid flow. *Int. J. Multiphase Flow*, Vol. 22, 473-83.
- [22] Dumbser M. , Iben U. , Munz C.-D. , 2013, Efficient implementation of high order unstructured WENO schemes for cavitating flows. *Comput. Fluids*, Vol. 86, 141-168 .
- [23] Edwards A.R., O'Brien T.P., 1970, Studies of Phenomena Connected with the Depressurization of Water Reactors. *J. British Nuclear Society*, Vol. 9, 125-35.
- [24] Emmert T., Lafon Ph., Bailly C., 2009, Numerical study of self-induced transonic flow oscillations behind a sudden duct enlargement. *Physics of Fluids*, Vol. 21, 106105.
- [25] Europlexus User's Manual, 2016. Technical Report, Joint Research Centre (JRC), Commissariat à l'énergie atomique et aux énergies alternatives (CEA). URL [http://europlexus.jrc.ec.europa.eu/public/manual\\_html/index.html](http://europlexus.jrc.ec.europa.eu/public/manual_html/index.html).
- [26] Fehlberg E., 1969, Low-order classical Runge-Kutta formulas with step size control and their application to some heat transfer problems. NASA Technical Report 315.
- [27] Gale J., Tiselj I., Horvat A., 2008, Two-fluid model of the WAHA code for simulations of water hammer transients. *Multiphase Science and Technology*, Vol. 20, 291-322.
- [28] Gale J., Tiselj I., 2008, Modeling of pressure undershoot and heat and mass transfer at negative pressures. *ASME FEDSM2005-77146*, pp. 807-14.
- [29] Goncalves E., Charrière B., 2014, Modelling for isothermal cavitation with a four-equation model. *Int. J. Multiphase Flow*, Vol. 59, 54-72.
- [30] Johnsen E., Colonius T., 2006, Implementation of WENO schemes in compressible multicomponent flow problems. *J. Comput. Phys.*, Vol. 219, 715-32.
- [31] Kapila A.K., Menikoff R., Bdzil J.B., Son S.F., Stewart D.S., 2001, Two-phase modeling of deflagration-to-detonation transition in granular materials: reduced equations. *Phys Fluids*, Vol. 13, 3002-25.
- [32] Kyriazis N., Koukouvinis P., Gavaises M., 2017, Numerical investigation of bubble dynamics using tabulated data. *Int. J. Multiphase Flow*, Vol. 93, 158-177.
- [33] Kunick M. et al., 2015, CFD Analysis of steam turbines with the IAPWS standard on the Spline-Based Table Look-Up Method (SBTL) for the fast calculation of real fluid properties. *Turbine Technical Conference and Exposition: Proceedings of ASME Turbo Expo 2015*.
- [34] Kunick M., Berry R.A., Martineau R.C., Kretschmar H.-J., Gampe U., 2017, Application of the new IAPWS Guideline on the fast and accurate calculation of steam and water properties with the Spline-Based Table Look-Up Method (SBTL) in RELAP-7. *Kerntechnik*, Vol. 82, 1-16.
- [35] LeVeque R., 2002, *Finite Volume Methods for Hyperbolic Problems*. Cambridge University Press, UK.
- [36] Linga G., Flatten T., 2019, A Hierarchy of Non-Equilibrium Two-Phase Flow Models. *ESAIM: Proceedings and Surveys*, Vol. 66.
- [37] Lochon H., 2016, Modélisation et simulation d'écoulements transitoires eau-vapeur. PhD thesis, Aix-Marseille.
- [38] Pelanti M., Keh-Ming Shyue K.-M., A mixture-energy-consistent six-equation two-phase numerical model for fluids with interfaces, cavitation and evaporation waves, *J. Comput. Phys.* Vol. 259, 331-57.
- [39] Pelanti M., Keh-Ming Shyue K.-M., A numerical model for multiphase liquid-vapor-gas flows with interfaces and cavitation. *Int. J. Multiphase Flow*, Vol. 113, 208-30.
- [40] Plesset M.S., Zwick S.A., 1954, The growth of vapor bubbles in superheated liquids. *J. Appl. Phys.*, Vol. 25, 493-500.



- [41] Press W.H., Teukolsy S.A., Vetterling W.T., Flannery B.P., 1997, Numerical Recipes. Cambridge University Press, USA.
- [42] Prosperetti A., Plesset M.S., 1978, Vapour-bubble growth in a superheated liquid. *J. Fluid Mech.*, Vol. 85, 349-368.
- [43] RELAP5/MOD3.3, 2001, code manual, Vol. I. Idaho Falls, USA
- [44] RELAP-7 Progress Report: FY-2015 Optimization Activities Summary. Report INL/EXT-15-36771, Idaho Falls, USA.
- [45] Riegel B., 1978, Contribution à l'étude de la décompression d'une capacité en régime diphasique. PhD thesis, Institut National Polytechnique de Grenoble.
- [46] Saurel R., Abgrall R., 1999, A Multiphase Godunov Method for Compressible Multiuid and Multiphase Flows. *J. Comput. Phys.*, Vol. 150, 425-67.
- [47] Saurel R., Gavriluk S., Renaud F., 2003, A multiphase model with internal degree of freedom, application to shock-bubble interaction. *J. Fluid Mech.*, Vol. 495, 283-321.
- [48] Saurel R., Le Metayer O., Massoni J., Gavriluk S., 2007, Shock jump relations for multiphase mixtures with stiffmechanical relaxation. *Shock Waves*, Vol.16, 209-32.
- [49] Saurel R., Petitpas F., Abgrall R., 2008, Modelling phase transition in metastable liquids. Application to cavitating and flashing flows. *J. Fluid Mech.*, Vol. 607, 313-50.
- [50] Saurel R., Petitpas F., Berry R.A., 2009, Simple and efficient relaxation methods for interfaces separating compressible fluids, cavitating flows and shocks in multiphase mixture. *J. Comput. Phys.*, Vol. 228, 1678-1712.
- [51] Skripov V.P., 1972, Metastable Liquids. Wiley, New York.
- [52] Skripov V.P., Sinicyn P.A. et al., 1980, Teplofizicheskiye Svoystva Zhidkostey v Metastabil'nom Sostoyanii. Atomizdat, Moskva.
- [53] Strang, 1968, On the construction and comparison of difference schemes. *SIAM J. Numer. Anal.*, Vol. 5, 506-17.
- [54] Suchanek M., Bartak J., 1989, Thermohydraulic Behavior of the Coolant in the Initial Phase of a Loss-of-Coolant Accident. *Proceedings of the second international symposium on multiphase flow and heat transfer*, 929-38.
- [55] Tiselj I., Petelin S., 1997, Modelling of Two-Phase Flow with Second-Order Accurate Scheme. *J. Comput. Phys.* Vol. 136, 503-21.
- [56] Tiselj I., Petelin S., 1999, Integration of the source terms in the two-fluid models. *NURETH 19*.
- [57] Tiselj I., Horvat A., Gale J., 2008, Numerical scheme of the WAHA code. *Multiphase Science and Technology*, Vol. 20, 323-54.
- [58] Toro E.F., 1997, Riemann Solvers and Numerical Methods for Fluid Dynamics. Springer-Verlag, Berlin, Heidelberg.
- [59] Toro E.F., Spruce M., Speares W., 1994, Restoration of the contact surface in the HLL-Riemann solver. *Shock Waves*, Vol. 4, 25-34.
- [60] Wagner W., Pruß A., 2002, The IAPWS Formulation 1995 for the Thermodynamic Properties of Ordinary Water Substance for General and Scientific Use, *J. Phys. Chem. Ref. Data*, Vol. 31, 387-535.
- [61] Wagner W. et al., 2000, The IAPWS Industrial Formulation 1997 for the Thermodynamic Properties of Water and Steam, *ASME J. Eng. Gas Turbines and Power*, Vol. 122, 150-182.
- [62] Ward C.A., 1977, The rate of gas absorption at a liquid interface. *The Journal of Chemical Physics*, Vol. 67, 229-35.
- [63] Wood A.B., 1930, A textbook of sound. G. Bell and Sons Ltd, London, UK.
- [64] Zein A., Hantke M., Warnecke G., 2010, Modeling phase transition for compressible two-phase flows applied to metastable liquids. *J. Comput. Phys.*, Vol. 229, 2964-98.